M.Sc. Thesis

Silicon MEMS Micro-Evaporator

Jun Hao

Electronic Components, Technology and Materials

Delft Institute of Microsystems and Nanoelectronics

Delft University of Technology

27-08-2009

Silicon MEMS Micro-Evaporator

Jun Hao

Bachelor of Science in Radio Engineering,

Master of Science in Circuit and System,

Southeast University, Nanjing, China

Supervisors:

Mr. M. Mihailović

Mr. C. M. Rops

Dr. J. F. Creemer

Prof. P. M. Sarro

Contents

Chapter 1

Introduction

1.1 What is a Micro-Evaporator?

With the miniaturization, in many chemical, pharmaceutical and biomedical processes, as well as in electronic devices, particularly in small satellites (figure 1.1), even small power dissipation may cause serious local heating. This heating keeps on increasing as the device dimensions decrease and energy density increases [1][2]. Therefore, the need for efficient cooling in these devices is very severe [3][4]. A micro-evaporator is a heat sink which deals with high heat fluxes by evaporating the liquid flowing in micro-channels. They are specifically of interest because of the great capacity on heat transfer and low mass flow [1].

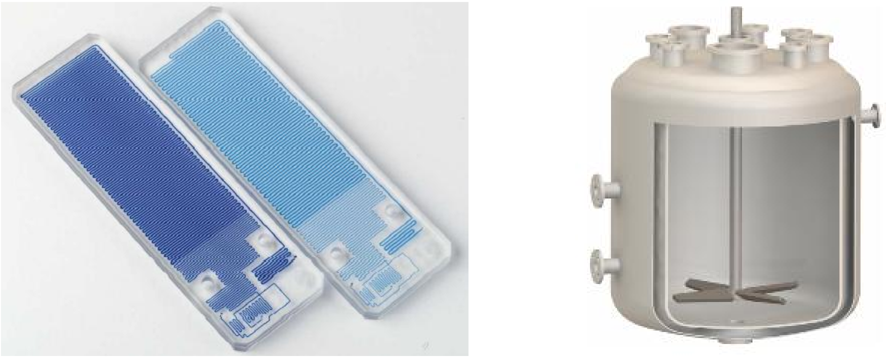

(*a*) Dolomite's microreactor chips (*b*) Typical pharmaceutical reactor

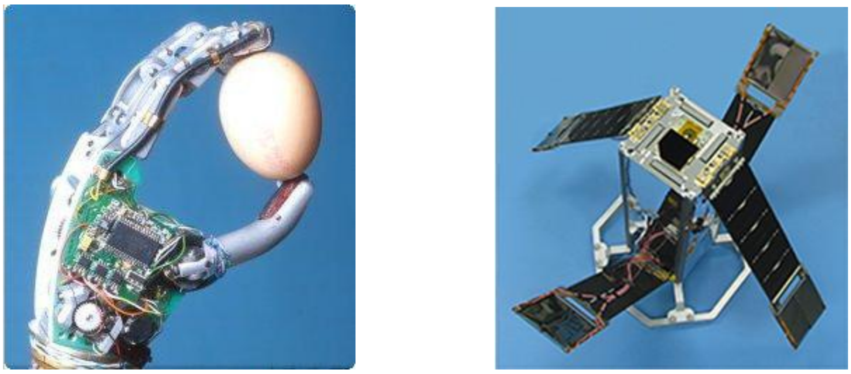

(*c*) Biomedical electronics (*d*) Delfi-C3

Figure 1. 1: Examples of processes causing heat

1.2 Why Micro-Evaporators?

1.2.1 Existing Heat Sinks and Heat Exchangers

Currently, there are numerous micro heat exchangers and micro heat sinks, which either absorb the heat with single-phase flow [5][6] or with two-phase flow [7][8][9], or are fabricated with solid materials such as copper [7][10]. Table 1.1 gives the dimensional parameters and performances of some existing heat sinks and heat exchangers (named from device A to device E), and one of the designs presented in this thesis – the device with 10 µm wide crosslinked channel structure (named device F).

Comparing these devices with each other, we can see silicon can be used to realize much smaller devices because of its compatibility with MEMS technology. Water is a preferred coolant in heat sinks which are based on two-phase flow, because it has a relatively large latent heat for evaporation, which is 2257 kJ/kg [11]. The latent heat for evaporation of e.g. commercially available liquid FC-22 is only about 8.6 kJ/kg [7].

Device	Material	Chip area (cm^2)	Height of chip (μm)	Height of fin (μm)	Width of channel (μm) (rectangular)	Width of fin (μm)	Diameter of channel (μm) (circular)	Distance between channels (μm)	Flow mechanism	Coolant	Flow rate (ml/h)	Heat flux (kW/m^2)
A-1981 [6]	Si	1		365	57	57			Single-phase	Water	3.1×10^4	7.9×10^3
B-1999 [7]	Cu		2.5×10^3				2×10^3	400	Two-phase	Water	1.08×10^5 / 2.16×10^5	2.29×10^3 / 4.34×10^3
B-1999 [7]	Cu		2.5×10^3				2×10^3	400	Two-phase	FC-72	1.08×10^6 / 2.16×10^6	830 / 1.16×10^3
C-2007 [8]	Cu	6.45	7×10^3	2.5×10^3	504	50			Two-phase	FC-77	3×10^3	213
D-2007 [5]	Si	1	500	400	50	50			Single-phase	Water	6×10^3	50
E-2007 [9]	Cu			10^3	500	10^3			Two-phase	Water	6.5×10^3	6×10^3
F-2009	Si	0.33	10^3	100	10 (crosslinked)	20			Two-phase	Water	0.6	29

Table 1. 1: Dimensions and performances of existing heat sinks and this design

1.2.2 Micro-Evaporators

When the liquid coolant reaches its saturation temperature, boiling occurs, which results in two-phase flow in micro-evaporators [12]. Boiling can absorb significant amounts of energy, as additional energy is required for the phase changing. This phenomenon enables the two-phase flow micro-evaporators to process higher heat dissipation.

As shown in table 1.1, although the designed micro-evaporator in this thesis project can not deal with as high heat fluxes as the existing heat sinks, the needed flow rate is a lot smaller than the flow rates in these heat sinks. And both the chip size and channel size of the micro-evaporator are also much smaller.

1.3 Miniaturization of Evaporator

This thesis demonstrates the miniaturization of the evaporators with fin structure fabricated in silicon with MEMS (microelectromechanical systems) technology. Silicon is an ideal material for miniaturizing micro-evaporators, due to its good thermal conductivity [11] and very good compatibility with MEMS technology. It can be etched in high aspect ratio fin-type geometries by deep reactive ion etching (DRIE). And the fin structure can be sealed by another wafer using direct wafer-to-wafer bonding [13].

The micro-evaporators in this thesis feature micrometre sized high aspect ratio channels and an embedded silicon heater to mimic external heat source. Moreover, the finned structures of our devices are a preferred way to increase the contact surface area without increasing the total footprint of the device. The micro-evaporators have been fabricated by direct wafer bonding and successfully tested with demineralized water as the coolant.

1.4 Outline of this Thesis

Chapter 2 introduces the theoretical background on heat transfer, pool boiling, and flow boiling in conventional channels and micro-channels.

Chapter 3 deals with heat transfer of fin structure and design of the micro-evaporators. The design of three different channel structured devices is introduced. And then the layout design and PCB design are presented.

Chapter 4 describes fabrication of the micro-evaporators. The main fabrication steps and the preparations for the fluidic measurement, such as dicing the whole bonded wafer into devices, gluing the needles into the devices and gluing the device to the PCBs are also given.

Chapter 5 presents the measurement of the micro-evaporators. First, heater characterization is introduced.

And then fluidic measurements of the devices and the test results analysis are given.

Chapter 6 contains a summary of the main conclusions and a number of recommendations for future work.

Chapter 2

Heat Transfer Theory

2.1 Introduction

This chapter introduces the theory background on heat transfer. First, the three different mode of heat transfer are introduced, which are conduction, convection and radiation, respectively. And then the boiling theory is discussed, which consists of pool boiling, and two-phase flow boiling. In the section of pool boiling, we focus on the different boiling regimes. Flow boiling in both conventional channels and micro-channels is introduced in the section of flow boiling.

2.2 Heat Transfer

Heat is the form of energy that can be transferred from one system to another as a result of temperature difference. The science that deals with the determination of the rates of such energy transfers is heat transfer. The transfer of energy as heat is always from the higher-temperature system to the lower-temperature system, and heat transfer stops when the two systems reach the same temperature, also known as the thermal equilibrium [14]. Heat transfer is commonly encountered in engineering systems (figure 2.1) and other aspects of life (figure 2.2). Actually the human body keeps on ejecting heat to the surroundings, and human comfort is closely related to the rate of this heat ejection (figure 2.3).

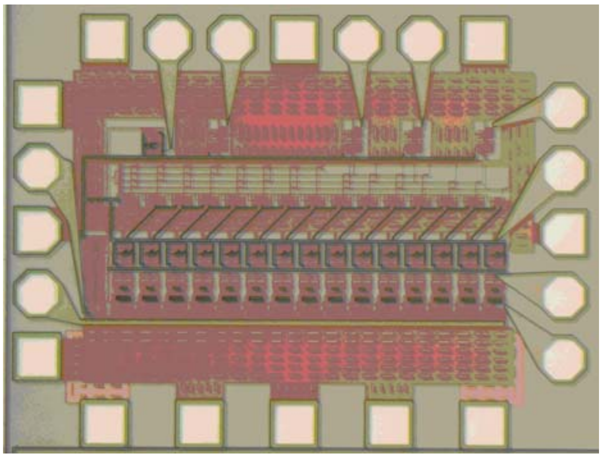

Figure 2. 1: Analog-to-digital circuit [15]

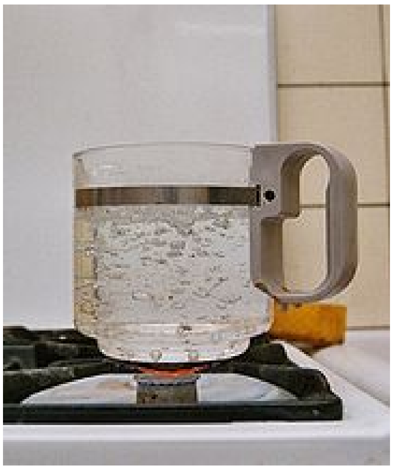

Figure 2. 2: Boiling water in a boiler

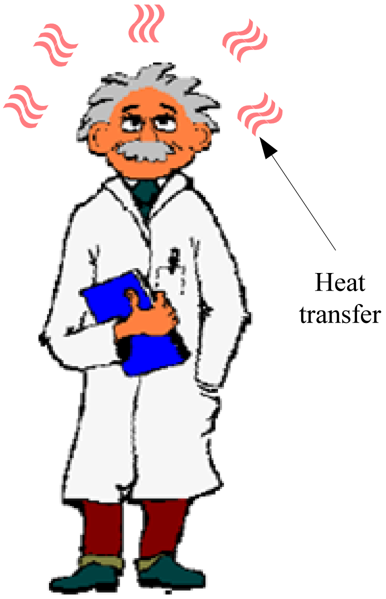

Figure 2. 3: Heat transfer from human body

Heat can be transferred in three different modes: conduction, convection, and radiation. Below we discuss these three modes briefly.

2.2.1 Conduction

Conduction is the transfer of heat by direct contact of particles of matter. Heat is transferred from the more energetic particles to less energetic ones. Heat transfer can occur in solids, liquids, or gasses. Liquids and gasses are also known as fluids. In solids, heat transfer is due to the combination of vibration of the molecules in a lattice and the energy is transferred by free electrons [14]. For example, cold drink in a can is finally warmed up to room temperature because of the conduction of aluminium (figure 2.4). Nevertheless, in fluids, assuming that there is no bulk, or macroscopic, motion [16], conduction is due to collision and diffusion of the molecules during their random motion.

In order to quantify the ability of a material to conduct the heat, thermal conductivity, also known as conductivity constant or conduction coefficient, λ, is employed, which is defined as the quantity of heat, Q, transmitted in time, t, through a thickness, L, in a direction normal to a surface of area, A, due to a temperature difference, ΔT [17]. It is a property of a material that is primarily dependent on the material's phase, temperature, density, and molecular bonding. Table 2.1 lists the thermal conductivity values of some materials at around 100 ºC.

The rate of heat conduction through a medium depends on the material of the medium, its geometry, its thickness, and the temperature difference across the medium. There is a salient example in our daily life. We wrap a hot water bottle with sponge, which has a thermal conductivity of 0.05 W/m·K [11], to keep the water warm. We know that the thicker the sponge, the smaller the heat loss. The lower the room temperature is, the more the heat loss is. And the larger the bottle is, which means the larger the contact area to the surroundings, the larger the rate of heat loss is.

Material	Thermal conductivity λ, (W/m·K)
Cu	393
Au	311
Si	98.9
Stainless-steel	16
SiO_2	1.5
H_2O(liquid)	0.68
H_2O(vapour)	0.025

Table 2. 1: Thermal conductivity values of some materials at 100 ºC [11]

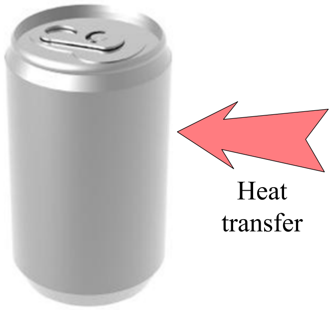

Figure 2. 4: Cold drink in aluminium can

It is possible to quantify the heat transfer processes in terms of rate equation. Figure 2.5 gives a large plane wall, which has a thermal conductivity λ, a thickness $\Delta x = L$, a surface area A_s and a temperature across it $\Delta T = T_2 - T_1$. The rate equation can be expressed as [16]:

$$q_x'' = -\lambda \cdot \frac{T_2 - T_1}{L} = -\lambda \cdot \frac{\Delta T}{\Delta x} \tag{2.1}$$

The heat flux q_x'' is the heat transfer rate in the x direction per unit area perpendicular to the direction of transfer. In the limiting case of $\Delta x \rightarrow 0$, the equation above reduces to the differential form:

$$q_x'' = -\lambda \cdot \frac{dT}{dx} \tag{2.2}$$

In the above equation dT/dx is the temperature gradient, which is the rate of change of T with x, at location x. Thus the power of the heat transfer q_{cond} can be calculated as:

$$q_{cond} = q_x'' \cdot A_s = -\lambda \cdot A_s \cdot \frac{dT}{dx} \tag{2.3}$$

This equation is called Fourier's law of heat conduction, which was first expressed by J. Fourier in his heat transfer text in 1822. It indicates that heat is conducted in the direction of temperature decreasing [14].

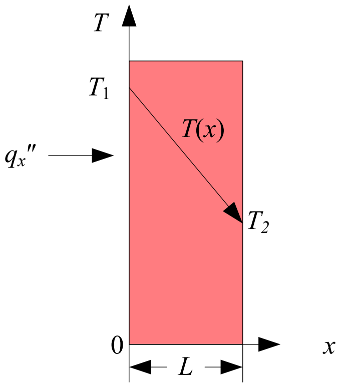

Figure 2. 5: One-dimensional heat transfer by conduction [14]

2.2.2 Convection

Convection is the mode of energy transfer between a solid surface and the adjacent liquid or gas that is in motion, and it involves the combined effects of conduction due to random molecular motion (diffusion) and fluid motion, due to bulk, or macroscopic, motion of the fluid [14][18]. If there is no motion of the fluid, the heat is transferred purely by conduction.

When convection occurs, first, energy is transferred to the fluid from the hot solid surface by random molecular motion. Then this energy is carried away from the surface by convection. The contribution of random molecular motion takes place near the surface ($y = 0$), where the fluid velocity is relatively low. Nevertheless the contribution due to fluid motion is that the heat taken away from the surface is swept down stream and absorbed by the fluid [16] (figure 2.6).

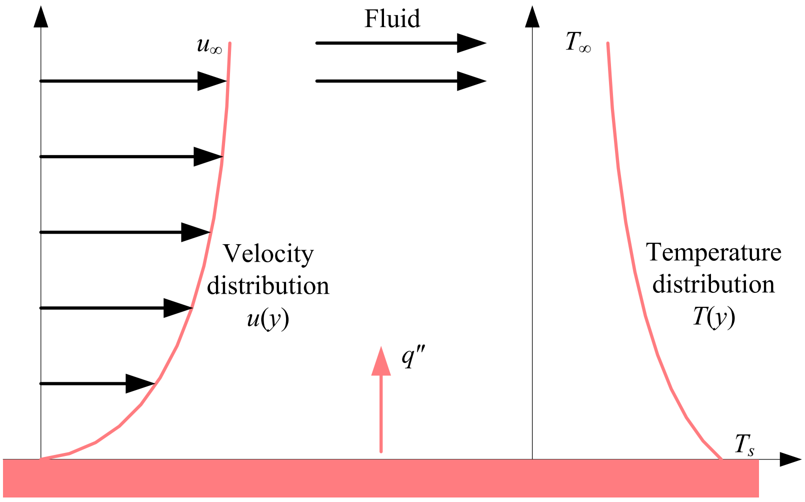

Figure 2. 6: Convective heat transfer from a hot surface to a flow [16]

There are two types of convection, natural convection and forced convection. Natural convection is induced by buoyancy forces due to density differences caused by temperature variation in the fluid. In contrast, forced convection is caused by external sources such as pumps and fans [19]. The convection heat transfer we discussed before is caused by conduction or bulk fluid motion, which is the internal thermal energy of the fluid. And no phase change occurs. Heat transfer processes with change of phase are also considered to be convection, for which there is also latent heat energy. Two typical changes of phase are of interest are boiling and condensation.

Consider a heated surface with an area A_s and surface temperature T_s, exposed in a fluid with a temperature T_∞ at a distance sufficient far away from the heated surface. Assuming the heat transfer coefficient is h, the convection heat power can be expressed as [19]:

$$q_{conv} = q'' \cdot A_s = h \cdot A_s \cdot (T_s - T_\infty) \tag{2.4}$$

In the equation above, q'' is the convective heat flux, which is the product of the heat transfer coefficient and temperature difference between the surface and fluid. Table 2.2 gives the typical values of the convection heat transfer coefficient.

Types of convection	Heat transfer coefficient h (W/m^2·K)
Free convection	
Gases	2 – 25
Liquids	50 – 1000
Forced convection	
Gases	25 – 250
Liquids	100 – 20,000
Convection with phase change	
Boiling or condensation	2500 – 100,000

Table 2. 2: Typical values of heat transfer coefficient [18]

2.2.3 Radiation

Radiation is the energy emitted by matter in the form of electromagnetic waves (or photons) as a result of the changes in the electronic configurations of the atoms or molecules [20]. Differing from conduction and convection, the energy of radiation is transferred by electromagnetic waves or photons, thus no transfer medium is necessary for radiation. Actually radiation can occur even more efficiently in a vacuum. An explicit example in our daily life is that the energy from the sun is transported by radiation through the vacuum in space.

Thermal radiation is one form of energy radiation that the energy emitted by bodies that are at nonzero temperatures [21], which may take place from solid surface, and liquids and gasses as well. Thermal radiation is a volumetric phenomenon. However, it is usually considered to be a surface phenomenon, which is that the thermal energy of matter bounded by the surface is emitted through the surface. Stefan-Boltzmann law can be used to quantify the maximum surface emissive power [20]:

$$q_{emit,\max} = \sigma \cdot A_s \cdot T_s^4 \tag{2.5}$$

In this equation, σ is the Stefan-Boltzmann constant ($\sigma = 5.67 \times 10^{-8}$ W/m^2·K^4), A_s is the surface area, and T_s is the absolute temperature of the surface. Such an ideal surface is called blackbody. However, the radiation emitted by a real surface is less effective than by a black body, the power of which can be expressed as (figure 2.7) [20]:

$$q_{emit} = \varepsilon \cdot \sigma \cdot A_s \cdot T_s^4 \tag{2.6}$$

In this equation, ε is emissivity of the real surface, which is smaller than 1. The emissivity values of some material surfaces are listed in table 2.3.

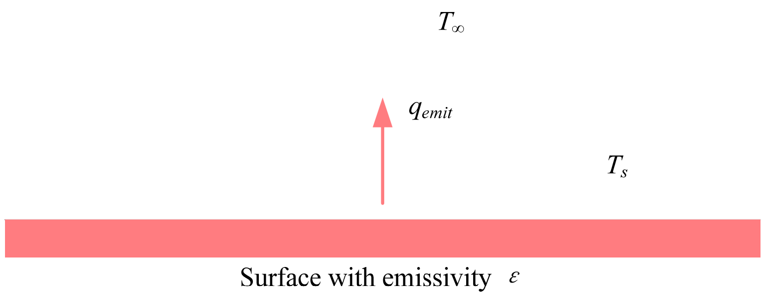

Figure 2. 7: Radiation from a hot surface

Material	Emissivity ε
Aluminium foil	0.07
Anodized aluminium	0.82
Polished copper	0.03
Polished silver	0.02
Polished stainless steel	0.17
Black paint	0.98
White paint	0.90
White paper	0.92 – 0.97
Asphalt pavement	0.85 – 0.93
Red brick	0.93 – 0.96
Human skin	0.95
Wood	0.82 – 0.92
Soil	0.93 – 0.96
Water	0.96
Vegetation	0.92 – 0.96

Table 2. 3: Emissivity of some materials [20]

In contrast, radiation can also incident from the surroundings to the surface. A portion or all of the incident radiation is absorbed by the surface. For a surface, which has absorptivity α, the power absorbed by the surface can be expressed as:

$$q_{abso} = \alpha \cdot q_{ince} \tag{2.7}$$

In this equation, q_{abso} is the absorbed power of the surface, and q_{ince} is the incident power from its surroundings.

The difference between the emitted power from the surface and the absorbed power from the surroundings is the net radiation heat transfer. The net radiation heat transfer can be expressed as:

$$q_{radi} = q_{emit} - q_{abso} = (\varepsilon - \alpha) \cdot \sigma \cdot A_s \cdot (T_s^4 - T_{sur}^4) \tag{2.8}$$

In this equation T_{sur} is the temperature of the surroundings.

If we assume that a heated surface is exposed in gas, and also take the convection heat transfer into account, the total power of the heat transfer is the sum of the convection power and the net radiation power of heat transfer, which can be expressed as [21]:

$$q_{total} = q_{conv} + q_{radi} = h \cdot A_s \cdot (T_s - T_\infty) + (\varepsilon - \alpha) \cdot \sigma \cdot A_s \cdot (T_s^4 - T_{sur}^4) \tag{2.9}$$

2.3 Boiling

As we mentioned in Section 2.2.2, boiling and condensation are two special cases of convection heat transfer of interest. In this section, we discuss the boiling theories, including pool boiling and flow boiling. Just like evaporation, boiling is also a liquid-to-vapour phase change process, but unlike evaporation, boiling occurs at the solid-liquid interface instead of the liquid-vapour interface. At the solid-liquid interface, when the temperature of the solid surface T_s is higher than the saturation temperature of the liquid T_{sat}, boiling takes place (figure 2.8). The difference between T_s and T_{sat} is called the excess temperature ΔT_e. As expressed in equation 2.4, the heat flux is $q'' = h \cdot \Delta T_e$. This process is characterized by the formation of vapour bubbles, which grow and subsequently detach from the surface. During this process, first heat is transferred in a single phase, which is the heat needed to heat the liquid to the saturation temperature. As soon as boiling occurs, phase change takes place. The liquid turns to vapour, which requires extra energy h_{fg} the latent heat of vaporization (two phase). Table 2.4 gives the latent heat of vaporization of different liquids.

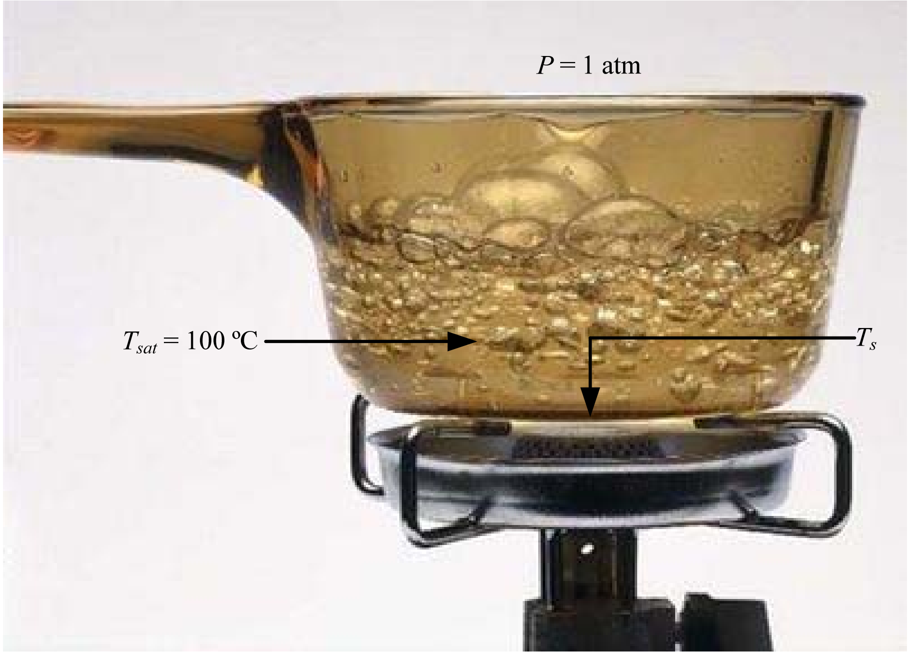

Figure 2. 8: Boiling in a pan

Material	Latent heat of vaporization h_{fg} (kJ/kg)
Helium	21
Freon refrigerant R-11	180
Oxygen	214
Hydrogen	461
Acetone	518
Carbon dioxide	574
Alcohol, ethyl (ethanol)	846
Alcohol, methyl (methanol)	1100
Water	2257

Table 2. 4: Latent heat of vaporization of some materials [22]

Boiling is classified as pool boiling and flow boiling. If the bulk fluid motion is due to free convection, boiling is called pool boiling or free convection boiling. In contrast, boiling is called flow boiling, which is known as forced convection boiling as well, if the bulk fluid motion is caused by external sources [23] (figure 2.9).

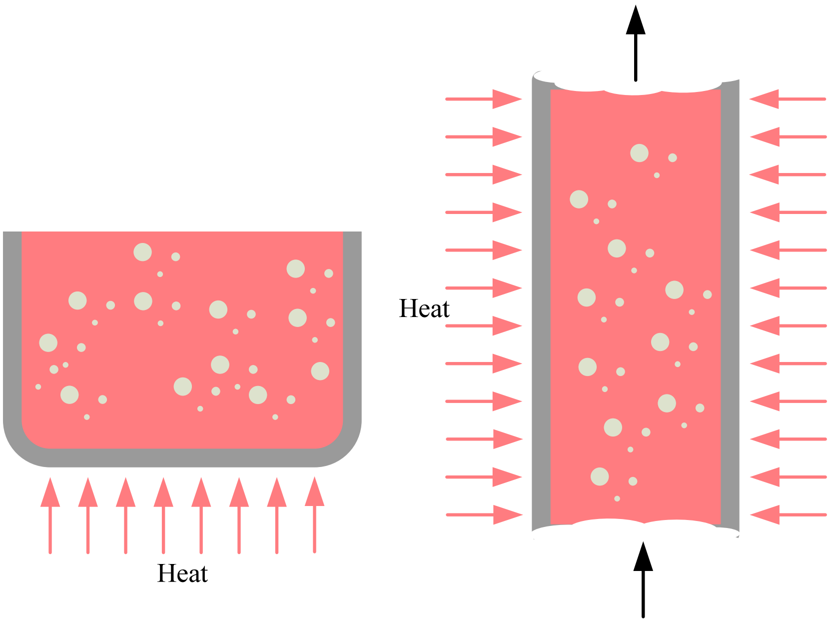

(*a*) Pool boiling (*b*) Flow boiling

Figure 2. 9: Classification of boiling on the basis of bulk fluid motion [23]

Pool boiling and flow boiling are further classified as subcooled boiling and saturated boiling. In subcooled boiling, the temperature of the main body of the liquid is lower than the saturated temperature and bubbles generated from the solid-liquid surface condense in the liquid. However, in saturated boiling, the temperature of the main body of the liquid is slightly higher than the saturation temperature of the liquid. Thus bubbles generated on the solid-liquid surface can be propelled through the liquid by buoyancy forces, and escape from the liquid surface (figure 2.10).

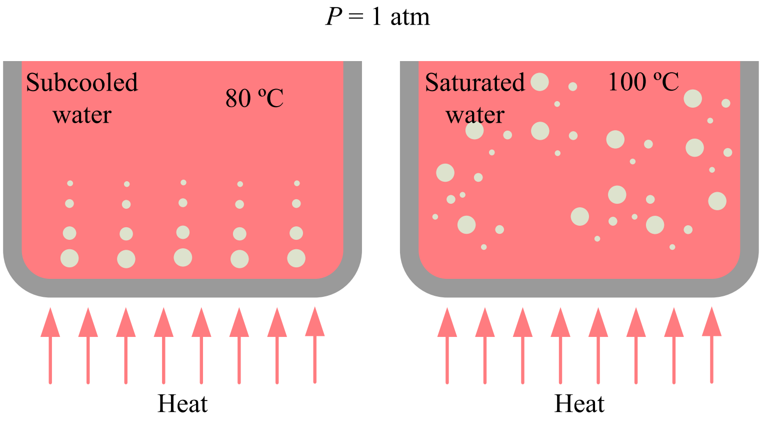

(*a*) Subcooled boiling (*b*) Saturated boiling

Figure 2. 10: Classification of boiling on the basis of bulk liquid temperature [23]

2.3.1 Pool Boiling

Pool boiling is the boiling in stationary fluid, which is not forced to flow by external means. The motion of the liquid is only caused by natural convection and the motion of the bubbles under the influence of buoyancy.

There are numerous pool boiling examples in our daily life and laboratories. For example, when you heat water in a beaker on a hot plate at standard atmospheric pressure, at the early stage of boiling (pre-mature boiling), you will only see some bubbles that stick to the bottom surface of the beaker. These bubbles are caused by the release of the dissolved air in the water, which should not be confused with the vapour bubbles or considered to be part of the boiling process. As the water temperature rises, chunks of water rolling up and down can be seen as a result of natural convection currents, followed by the first bubbles formed on the bottom surface of the breaker. The bubbles detach from the surface and rise with size shrinking because the water is cooler above. And eventually the bubbles condense in the cooler water. This is subcooled boiling as mentioned before, since the temperature of the main body of the water is still lower then the saturation temperature of water. As the temperature of the water further increases, the main body of the water reaches the saturation temperature, and you can see more vapour bubbles forming and rising to the top surface of the water, which is saturated boiling.

Modes of Pool Boiling

From equation 2.4, we note that the convective heat flux q'' depends on the excess temperature ΔT_e and the heat transfer coefficient h. Depending on the value ΔT_e, four boiling regimes of water are observed: free convection, nucleate boiling, transition boiling, and film boiling, as illustrated on the boiling curve in Figure 2.11.

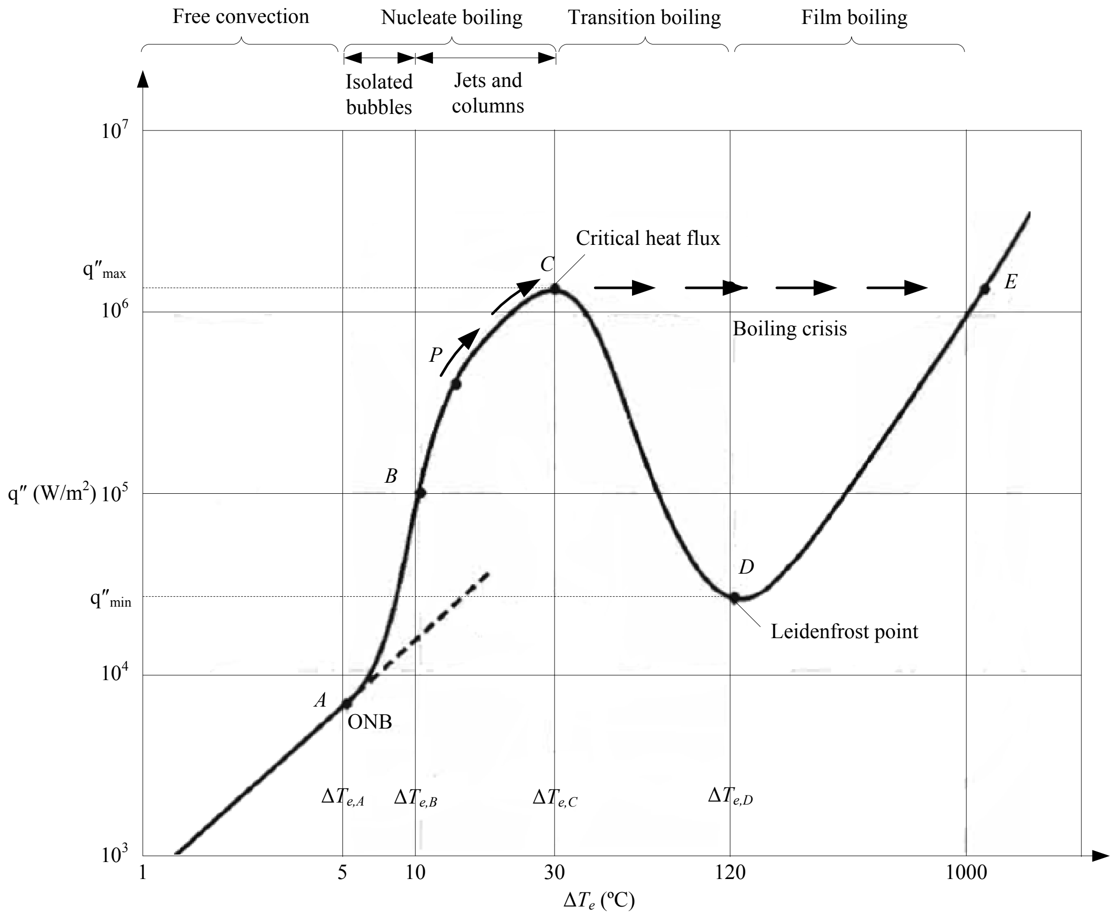

Figure 2. 11: Typical boiling curve for water at 1 atm pressure [24]

Free Convection Boiling (to point *A* on the boiling curve) [23][24]

Free convection boiling occurs in the temperature range $\Delta T_e < 5$ ºC. In this range, although bubbles start to form on the surface, they do not detach from the surface to the main body of the water; therefore it is a single phase convection process. The liquid is slightly overheated in a metastable condition and evaporates when it rises to the free surface of the water. Point *A* is called the onset of nucleate boiling, ONB.

Nucleate Boiling (from point *A* to point *C*) [24]

Nucleate boiling takes place in the temperature range $\Delta T_{e,A} \leq \Delta T_e \leq \Delta T_{e,C}$, where $\Delta T_{e,C}$ is around 30 ºC. This is a two-phase free convection boiling process, in which bubbles nucleate, grow, and depart from the heated surface (figure 2.12.a). And the intensity of the bubbles increases from point *A* to point *C*. This regime can be classified into two different regions. In region A-B, isolated bubbled are formed at nucleation sites and detach from the heated surface, then collapse in the water. The space left is filled by the water adjacent to the heated surface. The repetition of detachment of bubbles and substitution of water induce considerable fluid mixing near the heated surface and substantial increase of h and q''. In this regime, most of the heat is transferred by the motion of the liquid instead of the vapour bubbles.

In region B-C, the temperature of the heated surface is further increased and a significant amount of bubbles are generated from more activated nucleate sites, which form jets or columns and subsequently merge into slug of the vapour. The densely formed bubbles inhibit the motion of liquid near the heated surface. Point P on the boiling curve stands for the moment, when the heat transfer coefficient is a maximum. From this point the heat transfer coefficient h begins to decrease, but the excess temperature ΔT_e continues to increase. And because the relative increase of ΔT_e is more than the relative reduction of h, the heat flux q'', which is the product of ΔT_e and h, keeps on increasing, however, at a low speed. At point C, further increase of ΔT_e is balanced by the reduction of h, thus the heat flux achieves its maximum value q''_C, which is called the critical heat flux or maximum heat flux. For water, at atmospheric pressure it exceeds 1 MW/m^2.

Nucleate boiling is of great interest in practical application, because it can achieve the maximum heat flux at a relatively low ΔT_e, which is around 30 ºC. And the heat flux is considerably larger than those normal convection modes without phase change.

Transition Boiling (from point *C* to point *D*) [23][24]

The boiling mode in the temperature range $\Delta T_{e,C} \leq \Delta T_e \leq \Delta T_{e,D}$ is the transition boiling regime, unstable film boiling regime, partial film boiling, where $\Delta T_{e,D}$ is about 120 ºC. The formation of bubbles in this range is so intense, that a vapour film or blanket starts to form on the heated surface, which acts as an insulation due to the low thermal conductivity of the vapour comparing to water (figure 2.12.b). Thus the heat flux q'' starts to decrease from point C. In this regime, the boiling mode oscillates between nucleate boiling and film boiling.

Film Boiling (beyond point *D*) [23][24]

Film boiling happens when the excess temperature ΔT_e is higher than $\Delta T_{e,D}$, $\Delta T_e \geq \Delta T_{e,D}$. This mode is characterized by a stable layer of vapour that forms between the heated surface and the liquid, such that the bubbles form at the free interface and not at the heated surface (figure 2.12.c). Heat transfer from the heated surface to the water is carried out by conduction and radiation through the vapour. Point D on the boiling curve is termed as the Leidenfrost point, at which the heat flux is a minimum q''_D. As the temperature of the heated surface increases, radiation through the vapour film plays the main role in the heat transfer process and the heat flux increases with the increase of ΔT_e.

In this range, burnout phenomenon can happen, which can be explained as follows: In order to achieve the critical heat flux, the temperature of the heated surface T_s needs to be increased slightly. However when the critical heat flux is achieved, the fluid cannot hold this amount of energy. Therefore the heated surface stops absorbing the increased energy, causing the further increase of T_s. The temperature increases until the excess temperature of the surface reaches $\Delta T_{e,E}$, at which the heat flux is the same at point C. Obviously the temperature of the surface is much higher at point E than at point C, which is even higher than the melting point of the heater, resulting in burned out of the heater. Thus any attempt to increase the heat flux beyond q''_C will cause a sudden jump of the operation point from point C to point E. Therefore, point C is also called the burnout point, and the excess temperature should be kept slightly lower than $\Delta T_{e,C}$.

(*a*) Nucleate boiling

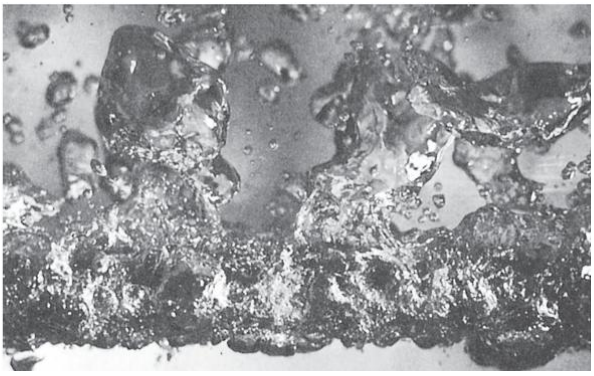

(*b*) Transition boiling

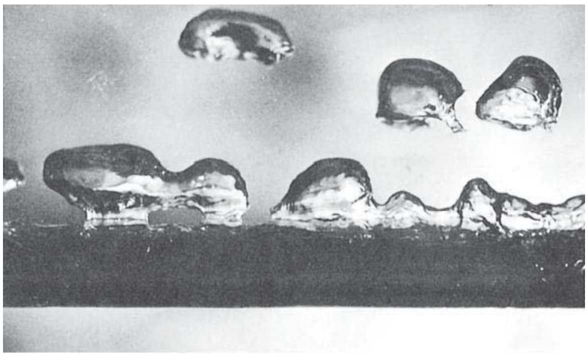

(*c*) Film boiling

Figure 2. 12: Different boiling regimes of methanol on a 1-cm-diameter horizontal copper tube [23]

2.3.2 Flow Boiling

In pool boiling, we consider that the liquid is motionless, and the vapour bubbles rise to the top due to buoyancy effects. Nevertheless, for flow boiling, or forced convection boiling, there is a directed (bulk) motion of the fluid caused by external means, such as a fan and a pump. The boiling in this case is the process combined by forced convection and pool boiling.

Flow boiling can be further separated into external flow boiling and internal flow boiling. External flow boiling happens over heated plates or cylinder, which is similar to pool boiling, but the added motion of liquid increases both the nucleate boiling heat flux and the critical heat flux considerably (figure 2.13). Figure 2.13 shows that the higher the flow velocity, the higher the heat flux of nucleate boiling regime and the critical heat flux. In experiments with water, critical heat flux as 35 MW/m^2 can be achieved comparing to the critical heat flux of 1.3 MW/m^2 of pool boiling at atmospheric pressure [4].

In internal flow boiling, there is no free surface for vapour bubbles to escape, thus both liquid and vapour are forced to flow together. Therefore, internal flow boiling is commonly referred to as two-phase flow. The two-phase flow in a tube also presents different regimes according to the relative amount of liquid and vapour phases.

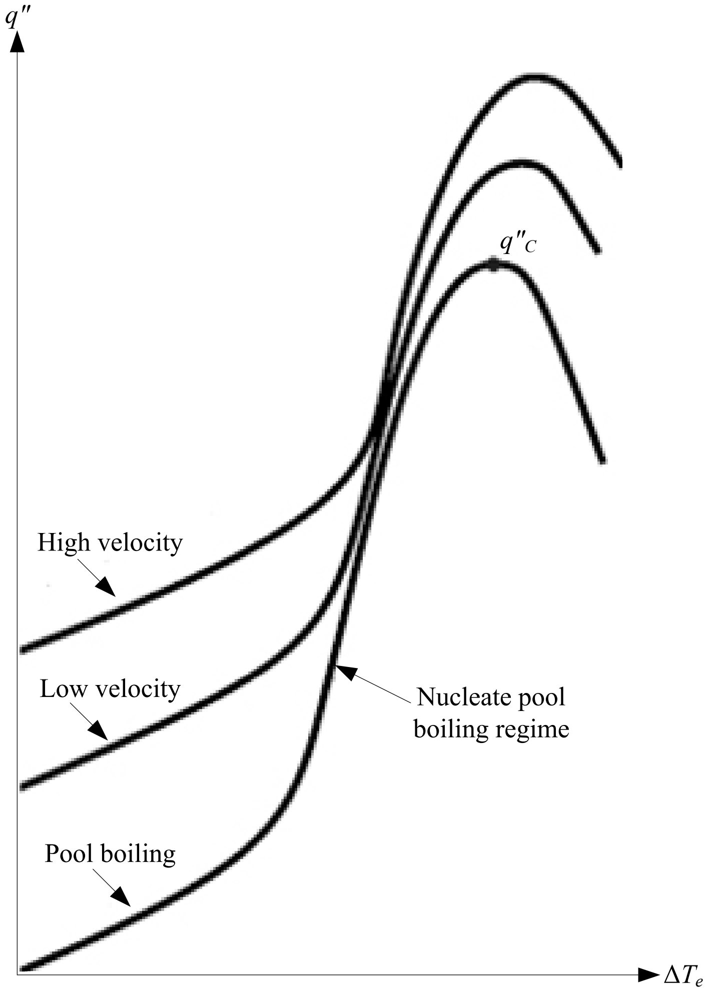

Figure 2. 13: The effect of forced convection on external flow boiling for different velocities [25]

Before discussing two-phase flow in channels, another concept needs to be introduced first, which is the hydraulic diameter, D_h. The hydraulic diameter can be expressed as [26]:

$$D_h = \frac{4A}{U} \tag{2.10}$$

In the above equation, A is the cross sectional area of a channel and U is the wetted perimeter of the cross section.

For a round channel having a diameter D, equation 2.10 can be written as:

$$D_h = \frac{4 \cdot \pi \cdot \left(\frac{D}{2} \right)^2}{\pi \cdot D} = D \tag{2.11}$$

For an annulus channel having an outer diameter D_o and an inner diameter D_i, equation 2.10 can be expressed in the form:

$$D_h = \frac{4 \times 0.25 \cdot \pi \cdot \left(D_o^2 - D_i^2 \right)}{\pi \cdot \left(D_o + D_i \right)} = D_o - D_i \tag{2.12}$$

For a rectangular channel, the hydraulic diameter can be expressed as:

$$D_h = \frac{4 \cdot L \cdot W}{2 \cdot (L + W)} = \frac{2 \cdot L \cdot W}{L + W} \tag{2.13}$$

In the above equation, L is the length of the cross sectional area of the channel and W is the width. If the length L is much greater than the width W, we have $D_h = 2W$.

Two-Phase Flow in Conventional Channels [25][27]

Figure 2.14 shows the different stages of flow boiling in a heated tube and the corresponding heat transfer coefficient along this tube. Initially, heat transfer to the subcooled liquid entering the heated tube is by liquid-phase forced flow convection. Further down the tube, vaporization is initialized adjacent to the heated wall, but subcooled liquid flows near the centre of the tube. This region is called subcooled flow boiling region. Further downstream, the core of the liquid reaches the saturation temperature. More bubbles start to form on the inner surface of the tube and detach into the main stream. Because the flow has a bubbly appearance, this regime is called bubbly flow regime, which is also the first stage of saturated flow boiling region. As the fluid is heated further, individual bubbles coalesce to form slugs of vapour. This regime is called slug flow regime, in which the slugs of vapour occupy up to half of the volume of the tube. Following this slug flow regime, it is the annular flow regime, in which the core of the flow consists of vapour only, and liquid is confined as film on the tube wall. In this region, a very high heat flux can be realized (figure 2.14). As the heating continues, this liquid film on the tube wall becomes thinner and thinner, and eventually dry spots appear on the inner wall of the tube and grow in size within a transition regime. The appearance of dry spots causes a sharp decrease in the heat transfer coefficient. This transition regime continues until the entire inner wall is completely dry-out; and the remaining liquid is in the form of droplets travelling at a high velocity in the core of the tube. This is the so-called mist flow regime. After all the droplets are completely vaporized, there is only superheated vapour left, which realized a second single-phase forced convection region. However, there is a significant difference in the density between the liquid and vapour phases, thus the velocity of the fluid also increased by several orders of magnitude between the first and second single-phase forced convection regions.

Note that, in both liquid forced convection region and vapour forced convection region, there are both only single-phase flows. Heat transfer in these two cases can be calculated using the appropriate relations for single-phase convection heat transfer. After subcooled flow boiling region and before vapour forced convection region, the flow appears in two phase. A crude estimate for heat flux in flow boiling can be obtained by simply adding the forced convection and pool boiling heat fluxes.

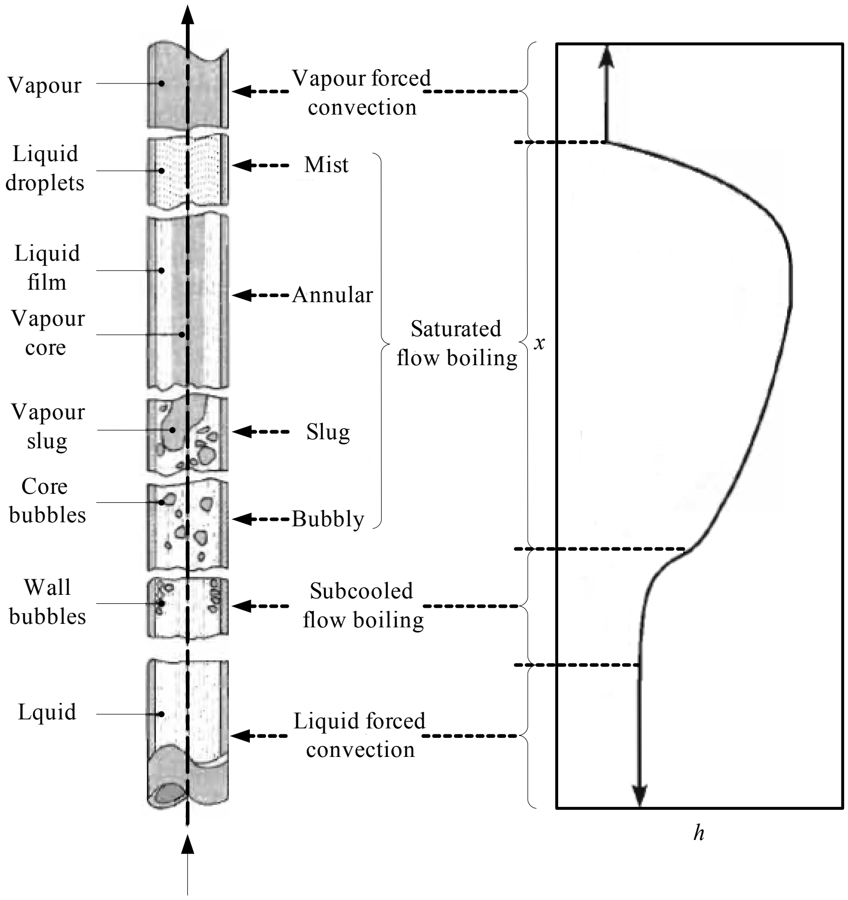

Figure 2. 14: Flow regimes for forced convection boiling in a tube [27]

Two-Phase Flow in Micro-Channels

Two-phase flow in micro-channels can be defined as the forced convection boiling of liquid through tubes having hydraulic diameters ranging from 10 μm to 200 μm [28], which results in extremely high heat transfer rates. In these situations, the characteristic bubble size can occupy a significant fraction of the tube diameter and the ‘Confinement number’ can become very large. Hence, the flow regimes will be different from those in conventional channels, including regimes where the bubbles occupy nearly the full diameter of the heated tube (annular flow boiling). This can lead to a dramatic increase in the heat transfer coefficient, *h* [29], corresponding to the peak in figure 2.14. But the same as in figure 2.14, the heat transfer coefficient decreases with increasing x.

It is of great importance that we have a good knowledge of dominant two-phase flow regimes in micro-channels. As shown in Figure 2.14, the heat transfer coefficient of two-phase flow in conventional channels is dictated by the flow regime, and the maximum value appears in annular flow boiling, which occurs after bubbly flow regime and slug flow regime. However, in micro-channels, one bubble can easily occupy a large portion of the entire channel during the phase change. Many research results already show that the bubbly flow regime and slug flow regime are either very short or even absent [30][31]. Therefore, in micro-channels, the annular flow regime can be formed immediately. Hence a major advantage of micro-channel heat sinks is that the maximum value of heat transfer coefficient can be achieved very quickly after the phase change starts. But it can also be regarded as the drawback of these device, because excessive boiling in micro-channels also cause dry-out spots, which leads to the decrease of the heat transfer coefficient.

The nucleation mechanism and the two-phase flow patterns in micro-channels are associated with the channel dimensions. According to the value of the hydraulic diameter, the channels can be classified into two types: sub-150 μm diameter channels, and sub-50 μm diameter channels. Figure 2.15 shows the liquid-vapour interfaces in a 113 μm diameter channel. Because of the small confined space in the micro-channels, a single bubble can consume the entire cross section and be forced to grow towards both ends of the channel. Even the tail of the bubble moves against the upstream liquid due to the sudden increase of the volume. This phenomenon is called reversed flow [32]. Once the downstream end of the bubble reaches the exit, the vapour discharges into the collector manifold, and the liquid pushes all the bubble out of the channel and refills the whole channel. At low heat fluxes, the flow regime switches between single phase flow and transient annular two-phase flow. However, at higher heat fluxes, the period of bubble generation becomes shorter and also more bubbles are generated simultaneously; as a result a steady annular flow appears with varying liquid layer thickness along the inner surface of the channel. In other words, there is no space for bubbly flow and slug flow to occur at the early stage of the phase change. Therefore, annular flow or mist flow develops immediately after onset of nucleate boiling.

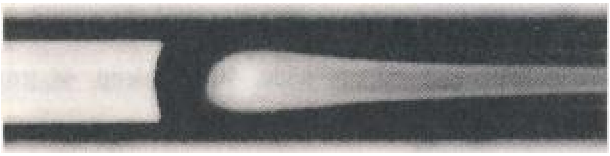

(*a*) The tail of the bubble

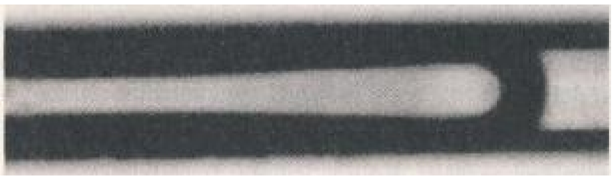

(*b*) The cap of the bubble

Figure 2. 15: The liquid-vapour interfaces in a 113 μm diameter channel [33]

Unlike in the sub-150 µm diameter channels, bubble growth and annular flow patterns cannot be captured in the sub-50 µm diameter channels. But only the oscillation of the liquid-vapour interface is formed directly as the result of the eruption boiling and fast vaporization, as show in figure 2.16 [33], which is also called explosive boiling. In the sub-50 µm diameter channels, the volume is even smaller, thus, a single bubble growth can affect the flow condition in the entire channel and the two-phase flow tends to shift to mist flow and explosive boiling. Figure 2.17 gives the scheme of explosive boiling [34]. The bubble is assumed to nucleate near the ONB point (figure 2.17a). Then the bubble starts quickly to grow to the channel size and an elongated bubble is formed. At this moment, there is still some amount of liquid in front of the bubble (figure 2.17.b). Figure 2.17c shows bubble venting, during which the bubble expands not only in the downstream but also in the upstream direction. Figure 2.17d shows the appearance of liquid droplets or clusters of liquid droplets on the wall after the bubble venting. After that, the pressure in the micro-channel decreases and water starts to move into it from the inlet. Figure 2.17e shows the start of a new cycle [30][34].

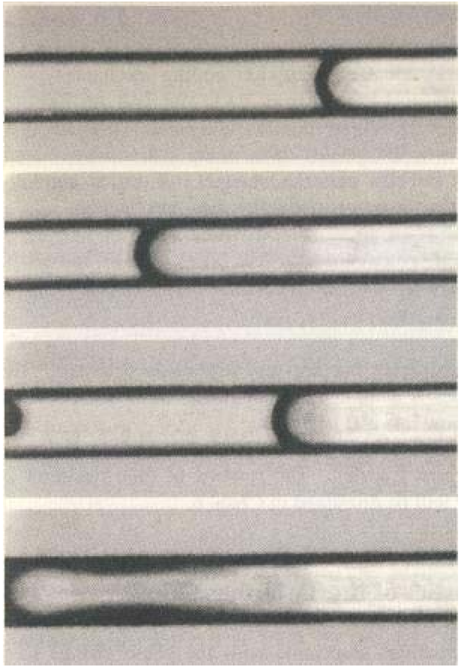

Figure 2. 16: Oscillation of the liquid-vapour interface

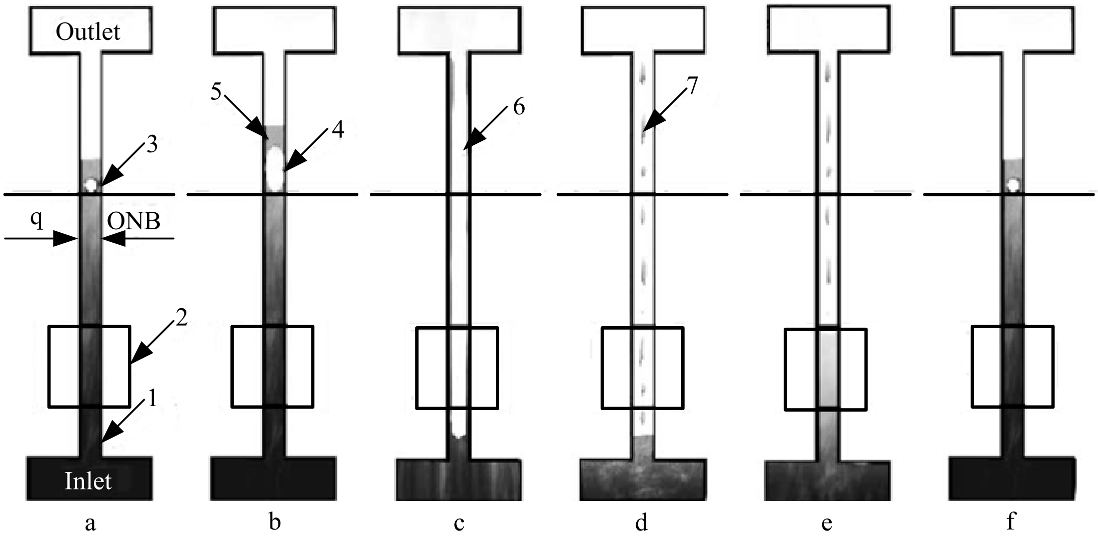

1. micro-channel, 2. main area of visual observation, 3. ONB point, 4. Elongated cylindrical bubble, 5. liquid in front of the bubble, 6. vapor, 7. liquid droplets and clusters

Figure 2. 17: Scheme of explosive boiling

2.4 Conclusions

In the chapter, the heat transfer theories were discussed. Three different heat transfer modes, conduction, convection and radiation were introduced. Conductive heat transfer is caused by direct contact of particles of matter, and from more energetic particles to less energetic ones. Convective heat transfer occurs between a solid surface and its adjacent fluid in motion. It is a combination of conduction due to random molecular motion and bulk fluid motion. Radiation is in the form of electromagnetic waves and does not need any mediums.

The boiling theories of pool boiling were also introduced. Different regimes of pool boiling were presented. Nucleate boiling can realize a critical heat flux, which appears at the excess temperature of about 30 ºC. Flow boiling can be classified into external flow boiling and internal flow boiling. External flow boiling is similar to pool boiling, but the critical heat flux increases with the flow velocity and appears at a higher excess temperature. Internal flow boiling, which is also known as two-phase flow, in conventional channels and micro-channels, was also studied. A very high heat flux can be realized by the annular flow in conventional channels. However in micro-channels, one bubble can occupy the whole channel and the explosive boiling dominates.

Chapter 3

Design of Micro-Evaporator

3.1 Introduction

In this chapter, design of the micro-evaporator is introduced. Fist, we discuss the structure design of the micro-evaporator. Since the channels play a relatively important role in the device, more attention is paid to the channel design. Three different channel structures are introduced. In order to mimic the processes which cause heating, a heater is integrated in the bulk silicon that serves as the structure material. The design of the heater is also introduced in this chapter. To fabricate the micro-evaporator, masks are needed to pattern the structures on silicon wafer, design of which is given in the layout design section. When testing the device, PCB served as in interface between the device, electrical source and multimeters. The last section gives the schematic of the PCB.

3.2 Structure Design

3.2.1 Fin Structure

Two-phase channel boiling is the main mechanism in the proposed micro-evaporator. In a two-phase flow micro-evaporator, parallel flow boiling channels may be regarded as a fin structure. Demineralized water is forced into the evaporator through the inlet, and is divided into the heated channels to absorb the heat by boiling. Finally, vapour leaves the evaporator through the outlet (figure 3.1a). Heat that is absorbed by the two-phase flow is generated in our demonstrator by electrical heating, in a heater that is integral part of the micro-evaporator structure (figure 3.1.b).

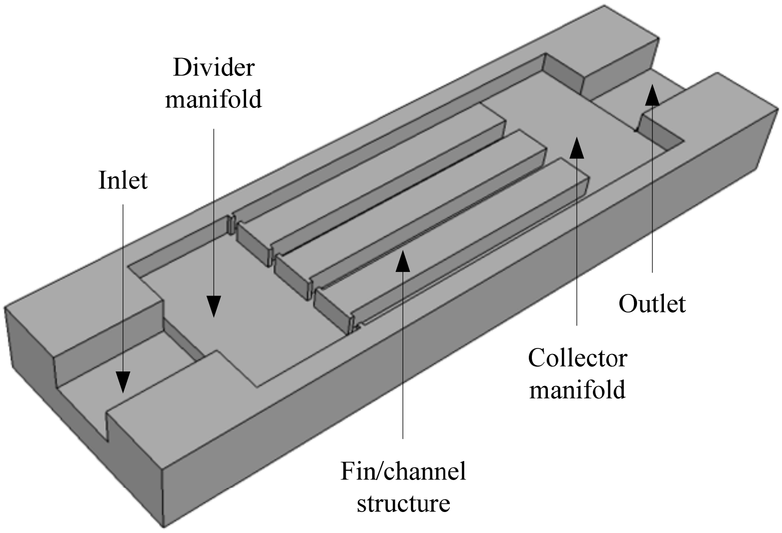

(*a*) Bottom side of the top half of the device

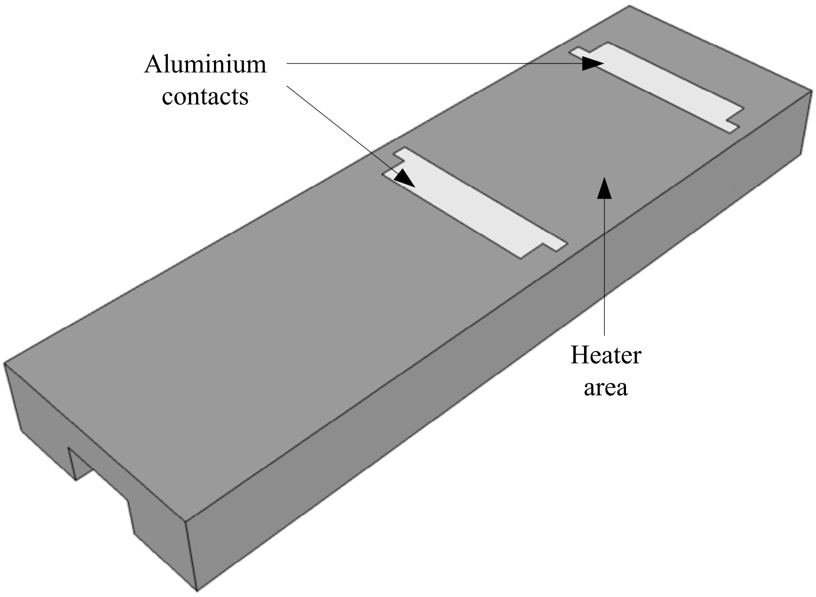

(*b*) Top side of the top half of the device

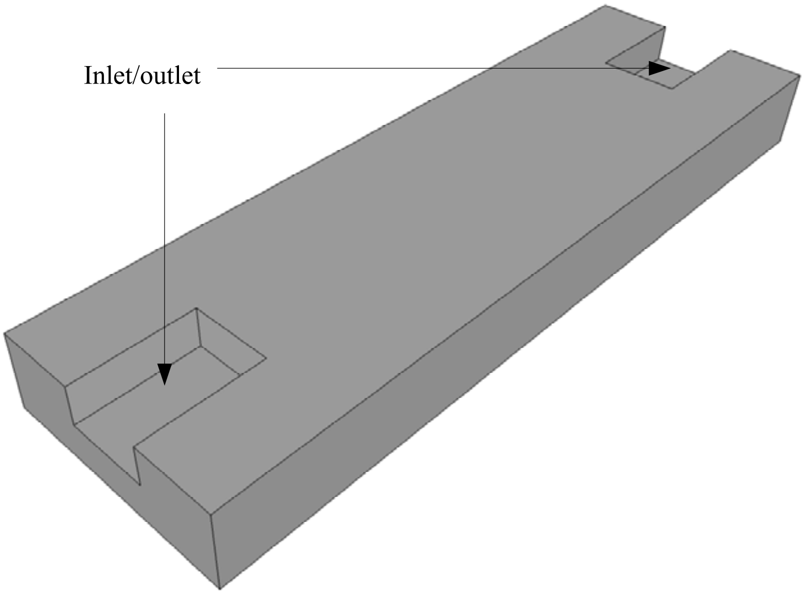

(*c*) Bottom half of the device

Figure 3. 1: 3-D sketch of micro-evaporator

A fin is a surface that extends from an object to increase the rate of heat transfer to or from the environment by increasing convection. Adding a fin to an object increases the surface area and can sometimes be an economical solution to enhance the heat transferring capacity of an object or surface. In order to simplify the calculation, a fin may be regarded as a two-dimensional structure (figure 3.2).

In figure 3.2, the base of the fin is assumed to be at a certain temperature T_{base}. Due to the heat transfer to the environment the temperature decreases along the fin. The temperature profile within the fin can be calculated by applying an energy balance over a part of the fin. The incoming power flow into the small partition can be expressed as [4]:

$$q'_{in} = -w \cdot \lambda \cdot \left. \frac{dT}{dx} \right|_{x} \tag{3.1}$$

In the above equation, w is the width of the fin, λ is the thermal conductivity of the fin (W/m·K), and *dT*/*dx* is the temperature gradient.

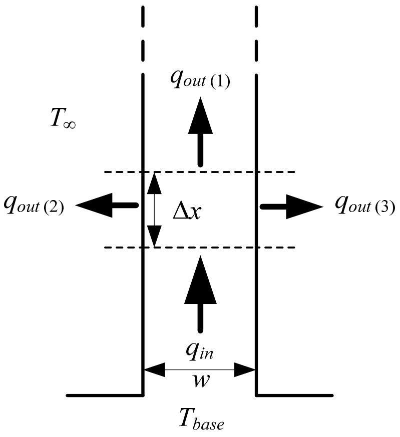

Figure 3. 2: Schematic of the cross section of a fin structure [4]

The outgoing power flows out the small partition consisting of two parts: power transferred due to conduction along the fin and heat losses due to convection to the ambient, which can expressed as [4]:

$$q'_{out} = -w \cdot \lambda \cdot \left.\frac{dT}{dx}\right|_{x+\Delta x} + 2 \cdot \Delta x \cdot h \cdot \left(T - T_\infty\right) \tag{3.2}$$

In the above equation, Δx is an infinitesimal small height partition of the fin, h is the heat transfer coefficient towards the ambient ($W/m^2 \cdot K$), T is the temperature of the fin, and T_∞ is the temperature of the ambient.

Because of the energy balance over the small partition, the power flows into this small partition should be equal to the power flows out of it [4]:

$$\begin{aligned} & q'_{in} = q'_{out} \\ & -w \cdot \lambda \cdot \left.\frac{dT}{dx}\right|_{x} - \left(-w \cdot \lambda \cdot \left.\frac{dT}{dx}\right|_{x+\Delta x} + 2 \cdot \Delta x \cdot h \cdot \left(T - T_\infty\right) \right) = 0 \\ & w \cdot \lambda \cdot \frac{d^2T}{dx^2} - 2 \cdot h \cdot \left(T - T_\infty\right) = 0 \end{aligned} \tag{3.3}$$

By assuming the base temperature of the fin to remain constant T_{base}, the above differential equation for an infinite long fin can be solved, and the following relation for the temperature profile within the fin is found (figure 3.3) [4]:

$$T(x) = \left(T_{base} - T_\infty\right) \cdot \exp\left(-\sqrt{\frac{2 \cdot h}{w \cdot \lambda}} \cdot x \right) \tag{3.4}$$

This profile is given schematically in figure 3.3.

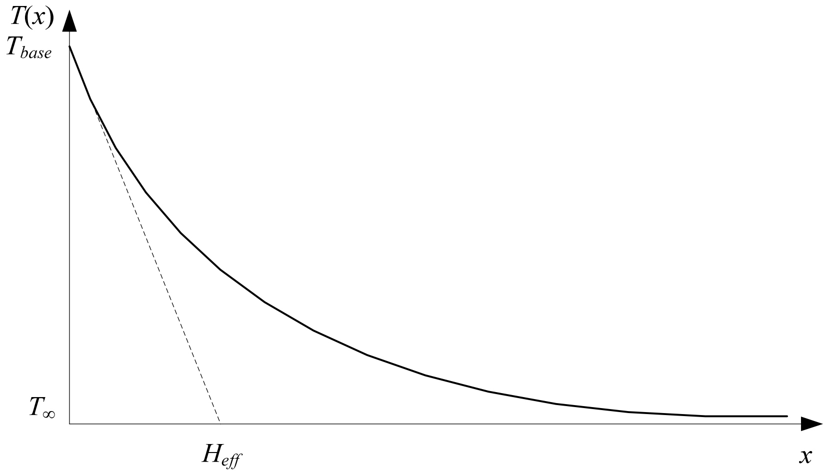

Figure 3. 3: Schematic of the temperature profile within an infinite high fin and its straight profile approximation [4]

The temperature difference between the fin and its ambient tends to zero at large distances from the base, which means at large distances from the base the parts of the fin do not contribute to the heat transfer. The effective height of the fin can be found by approximating the temperature profile with a straight line tangent to the temperature profile at the base of the fin (figure 3.3), which can be calculated as [4]:

$$\begin{gathered} -\sqrt{\frac{2\cdot h}{w\cdot\lambda}}\cdot x_{eff}=-1 \\ H_{eff}=x_{eff}=\sqrt{\frac{w\cdot\lambda}{2\cdot h}} \end{gathered} \tag{3.5}$$

The above equation shows that the effective height becomes larger when using a material with a higher thermal conductivity, λ. On increasing the width of the fin, a higher effective fin can also be made. However, note that increasing the width of the fin only increases the effective fin height by its square root, which means thin fins may have a larger aspect ratio.

From figure 3.3, it can be seen that the average temperature difference for a fin at effective height can be (under)estimated to be half of the temperature difference at the base of the fin, T_{base}-T_∞. The power transported through such a fin thus becomes [4]:

$$q'_{fin}=2\cdot H_{eff}\cdot h\cdot\frac{1}{2}\cdot\left(T_{base}-T_\infty\right)=H_{eff}\cdot h\cdot\left(T_{base}-T_\infty\right) \tag{3.6}$$

However, if the fins were not present, the power transported by the area occupied by the fin would be:

$$q'_w=w\cdot h\cdot\left(T_{base}-T_\infty\right) \tag{3.7}$$

The increase in heat transfer, q'_{fin}/q'_w, by using a fin with effective height is equal to the aspect ratio of the fin, H_{eff}/w (figure 3.4).

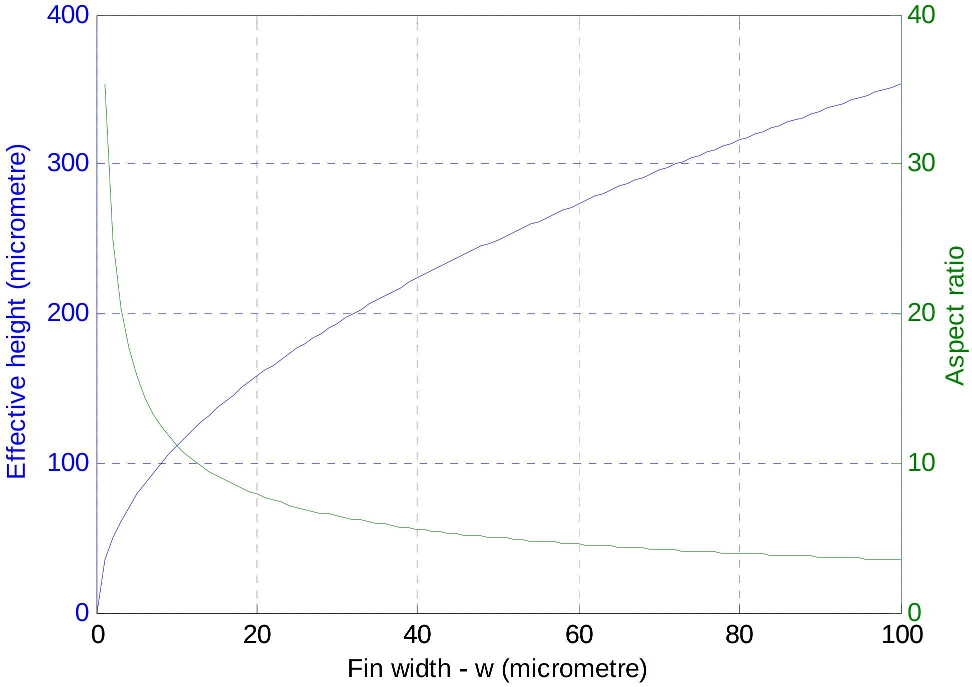

Figure 3. 4: Effective height and aspect ration as functions of fin width

$$\frac{q'_{fin}}{q'_{w}} = \frac{H_{eff}}{w} = \sqrt{\frac{\lambda}{2 \cdot h \cdot w}} \tag{3.8}$$

The above equation is only for a single fin, however in case multiple fins are placed next to each other the spacing in between the fins (channel width) should also be taken into account. The spacing in between the multiple fins is defined as the fin width multiplied by a factor, *k*. The heat transfer to the ambient by the wall between the fins can be assumed to be equal to the heat transfer to the ambient along the fins (figure 3.5).

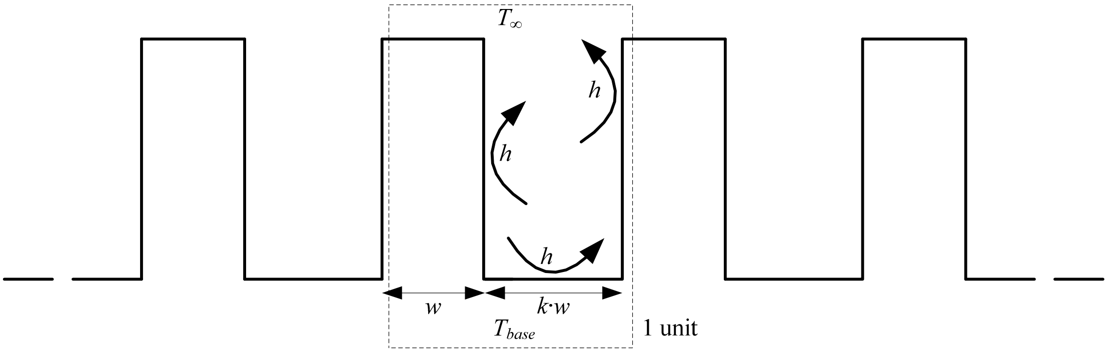

Figure 3. 5: Schematic of an array of fins and a unit cell of such an array

The total heat transfer of one single unit can be estimated by the following equation [4]:

$$q'_{fin\_unit} = 2\cdot H_{eff}\cdot h\cdot\frac{1}{2}\cdot\left(T_{base}-T_\infty\right) + k\cdot w\cdot h\cdot\left(T_{base}-T_\infty\right) = \left(H_{eff}+k\cdot w\right)\cdot h\cdot\left(T_{base}-T_\infty\right) \tag{3.9}$$

If the fins were not present, the heat transfer of one single unit would be:

$$q'_{w\_unit} = w\cdot h\cdot\left(T_{base}-T_\infty\right) + k\cdot w\cdot h\left(T_{base}-T_\infty\right) = (k+1)\cdot w\cdot h\cdot\left(T_{base}-T_\infty\right) \tag{3.10}$$

The fin structure effectiveness, which is the increase in heat transfer, q_{fin_unit}/q_{w_unit}, by using a fin with effective height, is equal to:

$$\frac{q'_{fin\_unit}}{q'_{w\_unit}} = \frac{\sqrt{\dfrac{w\cdot\lambda}{2\cdot h}}+k\cdot w}{\left(k+1\right)\cdot w} \tag{3.11}$$

The above equation shows that for specific material, *w* and *k* can be tuned to optimize the effectiveness of the fin structure. Figure 3.6 gives the effectiveness of the fin structure as a function of the width of the fin when *k* is set to different values.

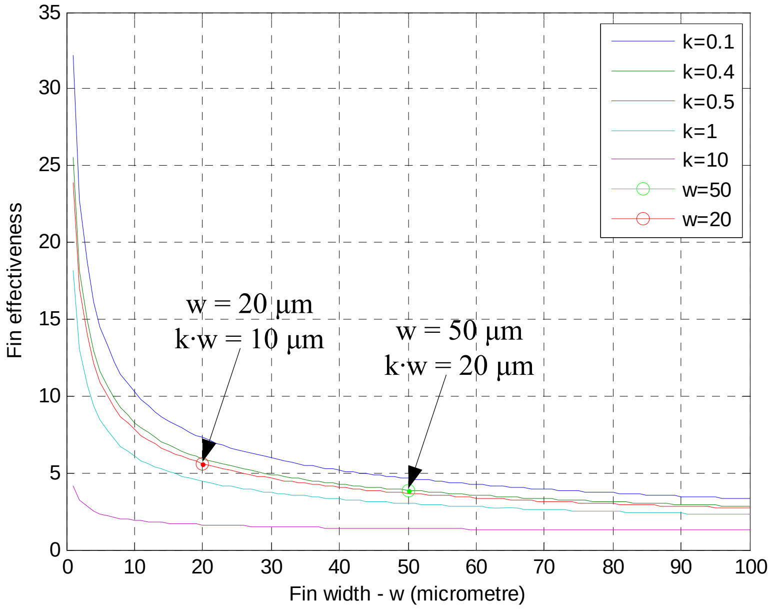

Figure 3. 6: Fin effectiveness as a function of fin width at different *k*

3.2.2 Structure Design

Three channel structures are proposed for the micro-evaporators, which are 10 µm wide straight channel structure, 20 µm wide straight channel structure, and 10 µm wide crosslinked channel structure.

These different structured devices are named type A, type B and type C. The size of the micro-evaporator chips is 10 mm × 3.3 mm, thus there are three different devices can fit on one lithography mask defining 10 mm × 10 mm die, which is the standard die size used in Dimes TC. Figure 3.7 depicts the top view of the devices and the channel structures of the proposed designs. The maximum heat flux obtained during flow boiling of water is about 1 MW/m^2, which happens at a 25 K excess temperature. Therefore the maximum heat transfer coefficient h is about 40 kW/m^2·K [4]. The thermal conductivity λ of silicon is about 100 W/m·K near the atmospheric boiling temperature of water.

Micro-Evaporator with 10 μm Wide Straight Channels (figure 3.7a)

For type A, the fin width w and the channel width $k{\cdot}w$ are designed as 20 μm and 10 μm, respectively. As shown in figure 3.6, if k increases, the effectiveness decreases. Thus, k should not be too large. However, if k is too small, the channel would be too narrow for boiling. According to equation 3.5, the related effective fin height, H_{eff}, is calculated to be 158 μm, and the total number of channels is 90. The length of the fin structure is 4 mm in total, and the height of the fin is designed to be 100 μm, which is still in the effective range. The channel entry is restricted to the width of 5 μm in order to prevent formed vapour bubbles from going back to the inlet and divider manifold.

Micro-Evaporator with 20 μm Wide Straight Channels (figure 3.7b)

For type B, the fin width w and the channel width $k{\cdot}w$ are designed as 50 μm and 20 μm. According to equation 3.5, the related effective fin height, H_{eff}, is calculated to be 250 μm, and the total number of channels is 39 here. The length of the fin structure and the height of the fin are also 4 mm and 100 μm, respectively. Because the width of the channels is 20 μm, thus there are two 5 μm wide entries for each channel with a 10 μm × 5 μm block in between.

Micro-Evaporator with 10 μm Wide Crosslinked Channels (figure 3.7c)

Figure 3.7c gives another channel structure. Instead of using straight channels, crosslinked channel structure is applied. After every 40 μm, there is another 20 wide channel perpendicular to the original channels, as shown in figure 3.7a. Because the pressure fluctuations here could be less than in the straight channel structures, restriction is not necessary in this structure.

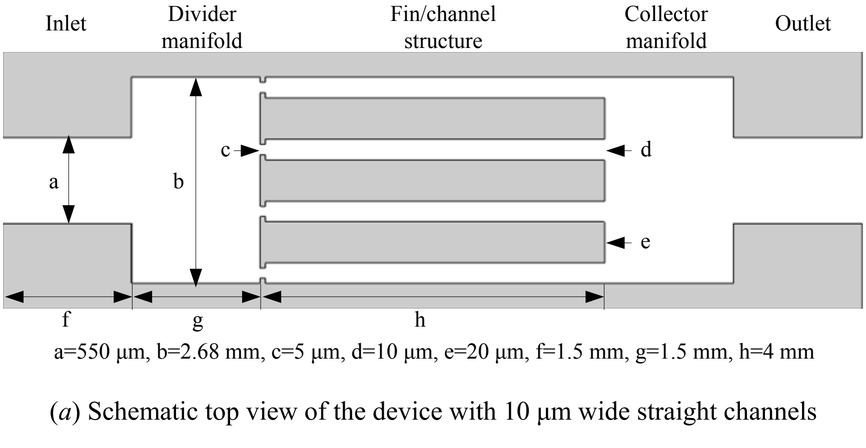

a=550 μm, b=2.68 mm, c=5 μm, d=10 μm, e=20 μm, f=1.5 mm, g=1.5 mm, h=4 mm

(*a*) Schematic top view of the device with 10 μm wide straight channels

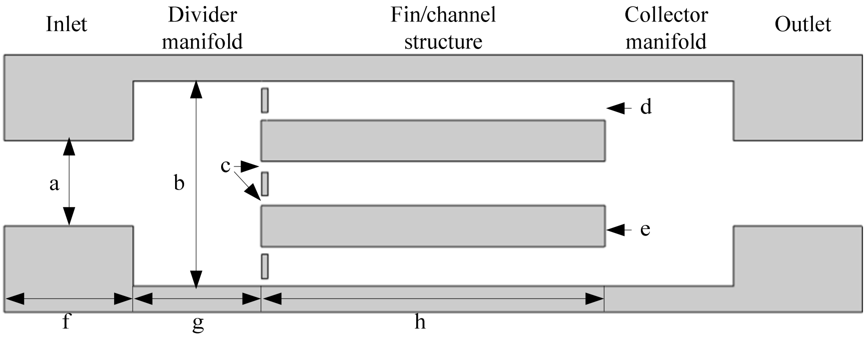

a=550 µm, b=2.68 mm, c=5 µm, d=20 µm, e=50 µm, f=1.5 mm, g=1.5 mm, h=4 mm

(*b*) Schematic top view of the device with 20 µm wide straight channels

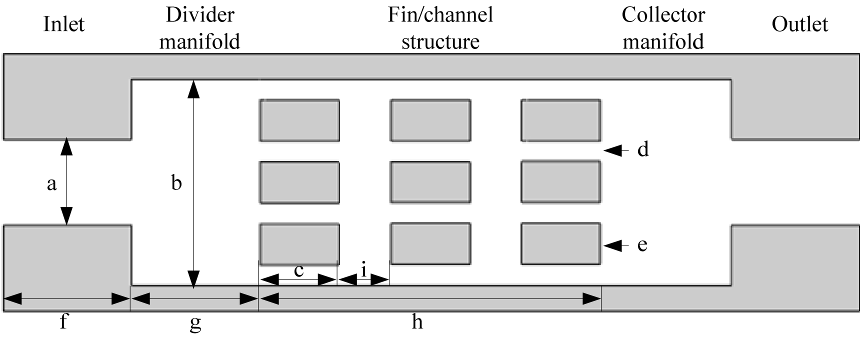

a=550 µm, b=2.68 mm, c=40 µm, d=10 µm, e=20 µm, f=1.5 mm, g=1.5 mm, h=4 mm, i=20 µm

(*c*) Schematic top view of the device with 10 µm wide crosslinked channels

Figure 3. 7: Top view of the devices with three different channel structures

The three different structured devices have the same inlet, outlet, divider manifold and collector manifold. As shown in figure 3.7, the divider manifolds and the collector manifolds are 1.5 mm long, 2.68 mm wide and 100 µm deep on the top half of the devices. Whilst the inlets and outlets are 1.5 mm long, 550 µm wide, but 275 µm deep on both halves of the devices, which means the cross section of the inlets and outlets is a 550 µm × 550 µm (figure 3.8)

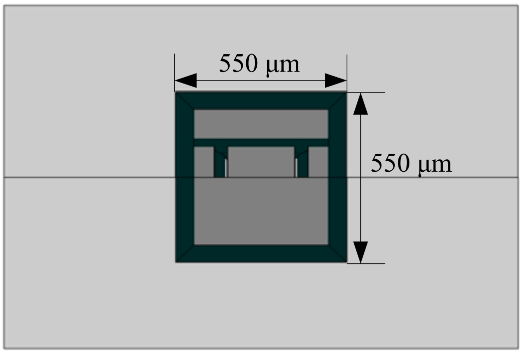

Figure 3. 8: Cross sectional view of the inlet

3.3 Heater Design

A heater is integrated in the bulk silicon that serves as the structure material. Aluminium contact pads are located on the top side of the device (figure 3.1b). The heater has two functions: the first one is to mimic processes which cause heating during the test; another function is to serve as a temperature sensor, due to the temperature dependent electrical resistance of silicon. The temperature of the channel structure can be monitored by measuring the resistance of the heater.

In order to mimic the processes causing heating, the heater should be able to supply enough power to evaporate the water flow though the channels. Thus, the power can be absorbed by the flow needed to be calculated, which consists of two parts, the heat loss to the ambient, $q_{heatloss}$ and the power to heat and evaporate the water flow, q_{evap}. The heat loss to the ambient can be regard as the convective heat transfer from the top surface, where aluminium contact pads are, to the air. The heat transfer coefficient of air is from 10 $W/m^2{\cdot}K$ to 100 $W/m^2{\cdot}K$ [11]. Assuming that the temperature of the top surface T_s is 125 ºC, and the room temperature T_{amb} is 20 ºC, the heat loss can be calculated as from 0.035 W to 0.35 W, according to equation 2.4. 0.35 W is used as the heat loss during the following calculation.

There are two methods to calculate the power to heat and evaporate the water flow, q_{evap}, the calculation of q_{evap} of the device with 10 µm straight channels is given as an example:

3.3.1 Basing on the Heat Transfer Theory

In Section 3.1, equation 3.9 presents the total heat transfer of one single unit. In our case, H_{eff} is 100 µm, $k{\cdot}w$ is 10 µm, h is 40 $kW/m^2{\cdot}K$, and $T_{base} - T_{sat}$ is 25 K, thus the total heat transfer of on single unit can be calculated as 110 W/m. As we mentioned before, there are 90 channels, and the total length of the channels is 4 mm. Therefore, the maximum total power can be transferred by the wall due to boiling is 39.6 W.

3.3.2 Basing on the Pressure Drop across the Device

As described in Chapter 2, when the hydraulic diameter of a channel is sub-50 µm, one bubble can occupy the whole channel. Thus the pressure drop, ΔP, over the channel can be regarded as the pressure drop over the bubble inside, which is given as [35]:

$$\Delta P = \frac{96}{\mathrm{Re}_{film}} \cdot \frac{L}{D_h} \cdot \frac{1}{2} \cdot \rho \cdot u^2 \tag{3.12}$$

In the above equation, L is the length of the channel; ρ is the density of water at 100 ºC; u is the velocity of the water thin film, but here we use the velocity of the water when entering the channel; Re_{film} is the Reynolds number given by equation 3.13; and D_h is the hydraulic diameter of the flow in channel. If the whole channel is occupied by one bubble, the flow can be regarded as a film flow. The thickness of the film flow is around $0.02 \cdot H_{eff}$[35], so the cross sectional area of the film flow can be approximated to be $2 \times 0.02 \cdot H_{eff} \cdot w$. According to equation 2.10, D_h is $0.04 \cdot H_{eff}$ here (figure 3.9).

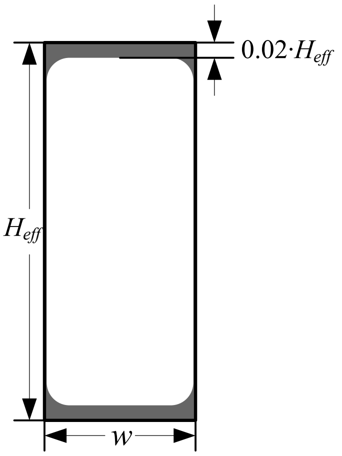

Figure 3. 9: Schematic of cross section of film flow in one channel

$$\mathrm{Re}_{film} = \frac{\rho \cdot u \cdot D_h}{\eta} \tag{3.13}$$

In the above equation, Re_{film} is the Reynolds number, and η is the viscosity of water at 100 ºC, which is 281.8×10^{-6} Pa·s. By substituting equation 3.13 into equation 3.12, the pressure drop can be presented as:

$$\Delta P = \frac{3 \times 10^4 \cdot \eta \cdot L \cdot u}{H_{eff}{}^2} \tag{3.14}$$

From equation 2.14, the equation for liquid velocity can be derived:

$$u = \frac{\Delta P \cdot H_{eff}{}^2}{3 \times 10^4 \cdot \eta \cdot L} \tag{3.15}$$

The volume flow rate, Q in one channel can be written as:

$$Q = u \cdot A_{cro} \tag{3.16}$$

In the above equation, A_{cro} is the cross sectional area of the annulus flow. The power for vaporization in one channel consists of two portions: heat for heating the water to its saturation temperature and power for liquid-to-vapour phase changing, which can be presented as:

$$q'_{evap\_unit} = \rho \cdot Q \cdot C_p \cdot (T_{sat} - T_{amb}) + \rho \cdot Q \cdot h_{fg} \tag{3.17}$$

In the above equation, C_p is the specific heat capacity of water, which is 4.183 kJ/kg·K at 20 ºC and 4.219 kJ/kg·K at 100 ºC; 4.187 kJ/kg·K is used for calculation. The latent heat for vaporizing water is 2257 kJ/kg, as described in Chapter 2.

If we assume the pressure drop over the channels is 1 bar, which is 10^5 Pa, the liquid velocity is 0.03 m/s, according to equation 3.15. The flow rate Q in one channel is 1.2×10^{-12} m^3/s (4.3×10^{-3} ml/h), which leads to q_{evap_unit} = 3.1 mW. Because there are 90 channels in total, the total power for vaporization at 1 bar pressure drop is 0.28 W, which is much smaller than 39.6 W (the total power can be transferred). Therefore 1 bar pressure drop is not enough to realize a flow rate, which can deal with the power of 39.6 W.

In fact, the power consumption of 39.6 W is the maximum power can be transferred by the fin/channel structures, which only occurs when nucleate boiling happens around all the solid-liquid surfaces. And the power of 0.28 W is the minimum power absorption, when all the channels are blocked by bubbles. Thus in the real case, 20 W is used as a criterion to design the heater and to make sure that the devices can work properly. The heater locates on the top side of the top half of the device, which is fabricated with a double side polished wafer. The heater is not centred, but is moved to the outlet in order to avoid boiling at the inlet and divider manifold (figure 3.10). For uniformity of the heat generation, the heater consists of a bulk silicon resistor, directly above and surrounding the channels.

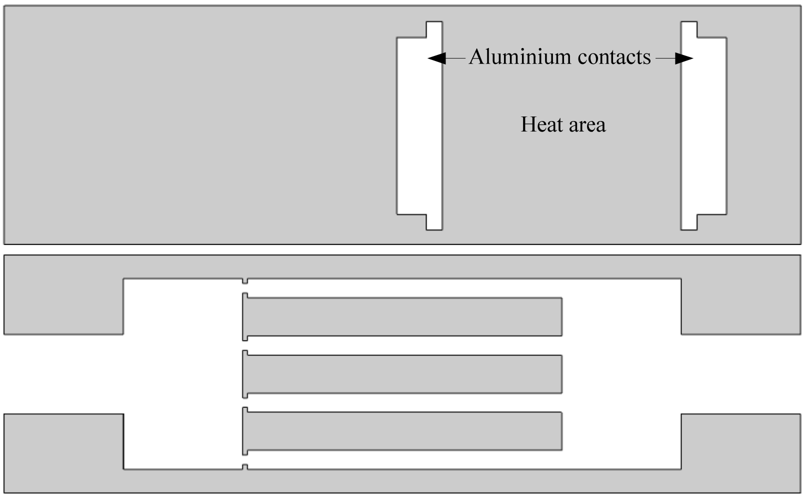

Figure 3. 10: Schematic of the location of the heater

The double side polished wafer has standard thickness, t, 525 μm and standard resistivity, ρ_{Si}, 3 Ω·cm at room temperature, which leads to a standard sheet resistance $R_{\square}$, 57.1 Ω/□ (equation 3.18). But because of the limitation of the technology, the thickness varies from 500 μm to 550 μm, and the resistivity varies from 1Ω·cm to 5Ω·cm, from which a range of $R_{\square}$, 18.2 Ω/□ ~ 100 Ω/□, can be derived. A voltage source which having a largest output 60 V is used to supply the voltage across the two aluminium contact pads. Therefore the size of the resistor is designed to be 2.7 mm × 2.7 mm, which is above and can surround the channels. At room temperature, the resistor can realized a resistance range, 18.2 Ω ~ 100 Ω, thus a voltage range, 19 V ~ 45 V, is needed to supply 20 W power. Therefore, a voltage source having a 60 V maximum output is enough.

Sheet resistance of a material can be calculated as [36]:

$$R_{\square} = \frac{\rho_{Si}}{t} \tag{3.18}$$

The maximum current density can safely go through aluminium is 10^5 A/cm^2 [37]. The aluminium contact pads are design to be 2700 μm × 515 μm, and 1.48 μm thick to hold the current density though these pads and enough bonding wires. There is also one 150 μm × 150 μm aluminium square pad at each side of the aluminium contacts, which serves as the wire bonding pads for voltage testing. More details are introduced in Chapter 4 and Chapter 5.

3.4 Layout Design

The micro-evaporator was fabricated in a four masks process. These masks are designed with L-Edit software and named MASK IMP_CO, MASK MET, MASK CH, and MASK IO, respectively, as shown in figure 3.11.

MASK IMP_CO is for defining the regions for boron implantation and for patterning contact openings, which is defined as a non-inverted and front side mask.

MASK MET is for patterning aluminium contact pads and the aluminium saw lines around the devices for dicing after fabrication, which is defined as an inverted and front side mask.

MASK CH serves for etching the channel structures, divider and collector manifolds, and the inlet and outlet 100 μm, which is defined as a non-inverted and back side mask, because these structures are patterned on the other side of the wafer.

MASK IO is for etching inlet and outlet 175 μm more (see chapter 4), which is also a non-inverted and back side mask.

In these masks, MASK IMP_CO, MASK MET and MASK IO are the same for three different devices, since these devices have the same structure for aluminium contact pads, inlet and outlet. But because each device has its own channel structure, the mask for patterning the channel structures has three different patterns (figure 3.11c). The zoom-in of the channel structures are also given in figure 3.11c, because the channels in microscale size cannot be seen in the original figure.

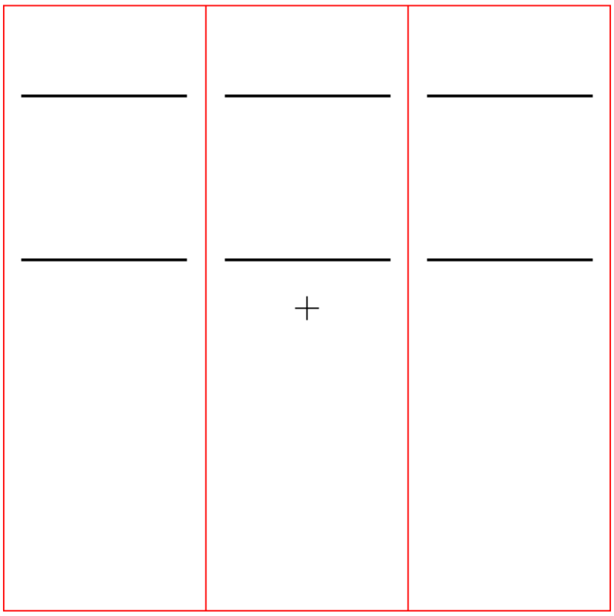

(*a*) MASK IMP_CO

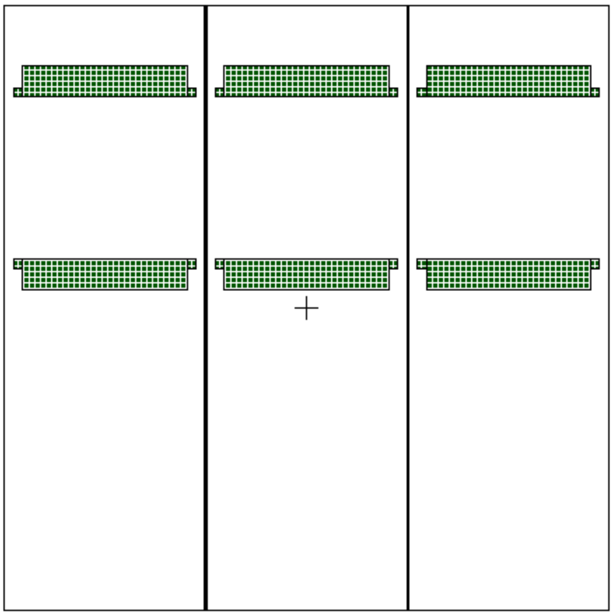

(*b*) MASK MET

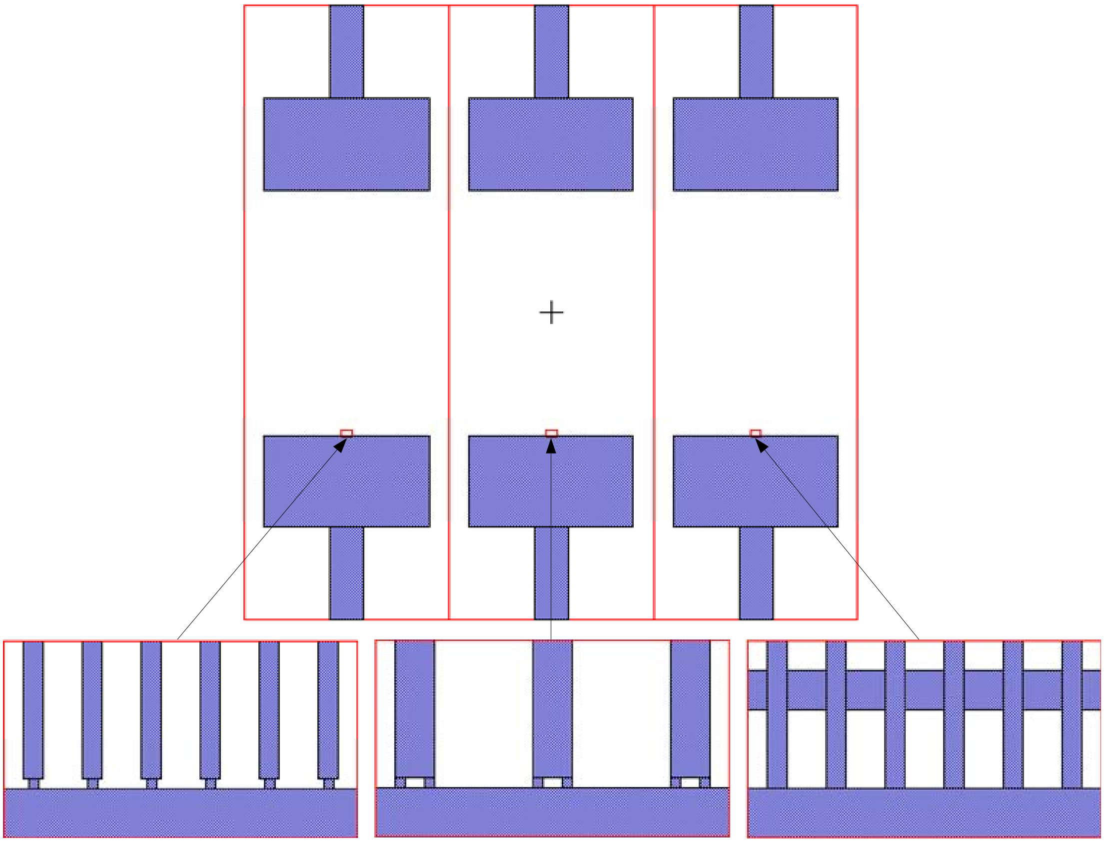

(*c*) Mask CH

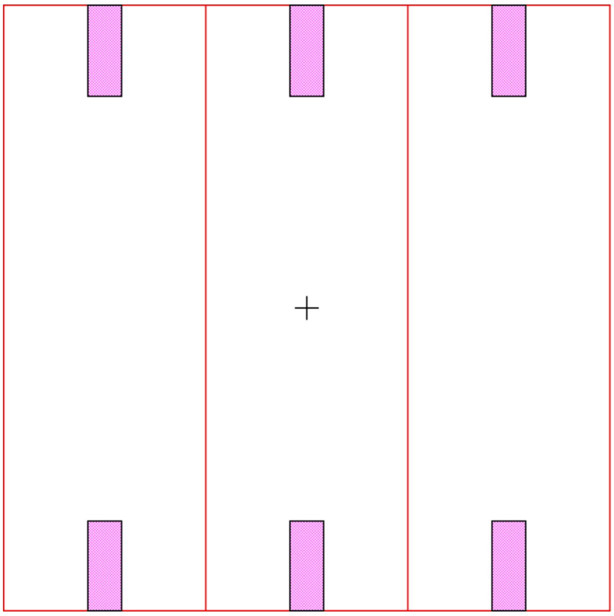

(*d*) MASK IO

Figure 3. 11: Four masks for micro-evaporator fabrication

3.5 PCB Design

In order to test the micro-evaporator, PCB is needed to serve as an interface between the electrical facilities, such as the voltage source, amperemeter and voltmeter, and the micro-evaporators. The PCB was designed with Protel DXP software. Figure 3.12 gives the schematic of the PCB. Current flows into this PCB through pad I+ and goes out though pad I-, and the voltage drop over the device is measured thought the pads V+ and V-. Since the signals goes though The PCB are only DC signals, there are no critical requirements on the shape or material, except the electro migration on the pads and connection wires. Bondable gold can be used to fabricate the pads and wires with a thickness from 0.3 µm to 0.5 µm. A safe value of maximum current density of gold conductors on a flat surface is 3.3×10^5 A·cm^2 [38]. Therefore a 2 mm wide wire is able to hold a current from 1.98 A to 3.3 A, which is much larger than the current needed to realized 20 W power.

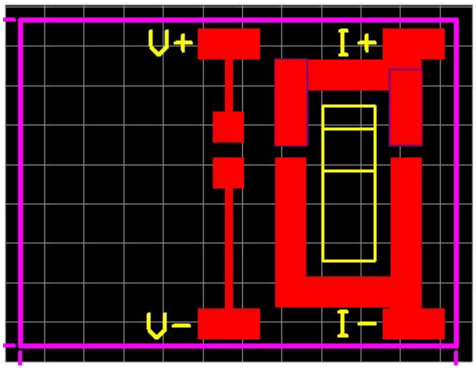

Figure 3. 12: Schematic of PCB

3.6 Conclusions

In this chapter, design of the micro-evaporators was introduced. First the fin structure theory was explained. Wide fins have higher effective height, but the effective height increase with the square root of the width, which mean narrow fins have larger aspect ratio. The fin structure effectiveness is a function of *k*, the ration between the width of the channels and the width of the fins. For a specific fin width, the smaller *k* is the more effective the fin structure is. Then three different structured channels were presented. A heater was designed to realize a 20 W power with the bulk resistance of the silicon. It has an area of 2.7 mm × 2.7 mm.

Four masks were designed to process the devices. And in order to test the devices, a PCB was also design to serve as an interface between the devices and the electrical facilities. Bondable gold was used as the material for pads on the PCBs.

Chapter 4

Fabrication of Micro-Evaporator

4.1 Introduction

This chapter deals with fabrication of the micro-evaporators. First, the fabrication of the devices is introduced, in which the main process steps are explained. And then, wafer dicing, gluing the inlet needles to the devices, gluing the devices to the PCB and wire bonding from the devices to the PCB are presented.

4.2 Fabrication of Devices

The micro-evaporator was fabricated in a four masks process, starting with a double-side polished wafer (further denoted as the top wafer) that is bonded to a single-side polished wafer (bottom wafer). Both wafers were p-type <100> single crystal wafers, 525 μm thick and 100 mm in diameter.

To perform direct wafer bonding, the bonding surfaces should be very smooth and free of particles. Therefore, a 300-500 nm thick wet thermal oxide layer is needed as the first step for both of the wafers to protect the bonding surfaces during processing (figure 4.1).

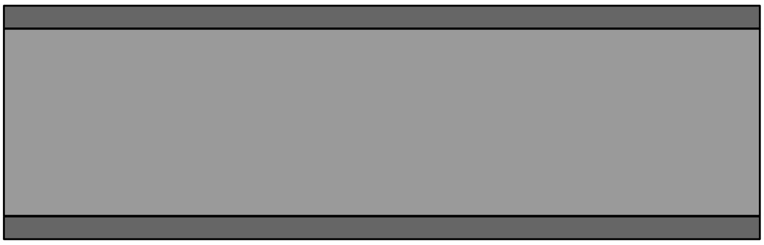

(*a*) Top wafer with 360 nm SiO_2 on both sides

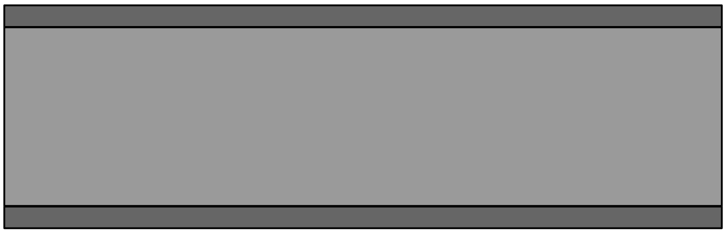

(*b*) Bottom wafer with 500 nm SiO_2 on both sides

Figure 4. 1: Wet oxidation on both sides of two wafers

Alignment marks, which are crucial for aligning the wafer with lithography masks, are then etched through the oxide layer and in the silicon.

On the top side of the top wafer, contact windows were opened in the oxide layer, by using MASK IMP_CO (figure 4.2a).

Silicon was doped by boron implantation (energy: 50 keV, dose: 1×10^{15} cm^{-2}) to make low-ohmic contact between the aluminium thin film and the silicon bulk. Implantation was performed through the thin SiO_2 layer. This SiO_2 layer was grown by thermal oxidation and is 30 nm thick (figure 4.2b, figure 4.2c). It acted as a dirty barrier, because implantation is a high-energy process, and accelerated ions sputter metal atoms from the implanter hardware. The thin SiO_2 layer prevented these metal atoms from penetrating into silicon. In the post implantation clean, this thin oxide layer and the metal atoms in it could be easily removed by a HF dip etch. This thin oxide layer also randomized incoming ions to avoid channelling phenomenon [13]. Implantation was also performed by using MASK IMP_CO.

Implantation was followed by the annealing step (20 min at 950 ºC in argon gas) to fix the amorphization caused by implantation and to activate the dopants. After that, HF dip etch was applied to remove 30 nm of silicon oxide from the contact windows.

Metalization was performed by sputter-deposition of 1.475 µm think aluminium layer (which contains 1% of silicon). Aluminium was patterned with the MASK MET by the wet etching process (figure 4.2e, figure 4.2f). Alloying step was performed at 400 ºC to improve the electrical contact between aluminium and silicon.

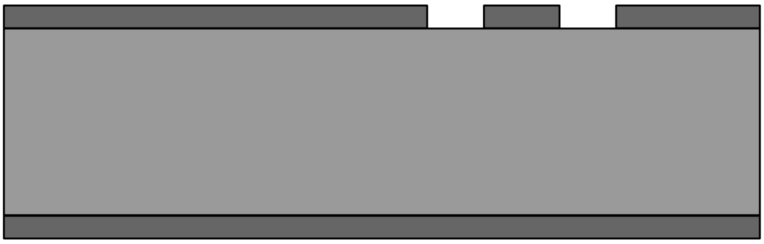

(*a*) Contact openings on SiO_2 layer

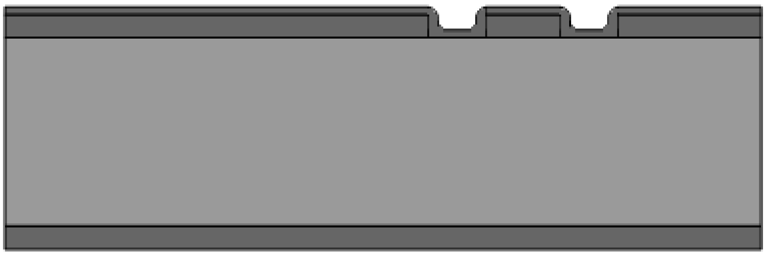

(*b*) 30 nm thermal SiO_2 layer for implantation

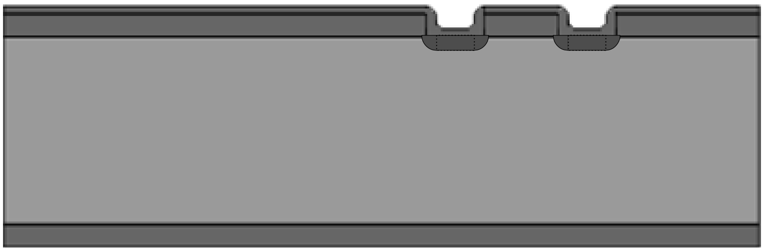

(*c*) Boron dopant implantation

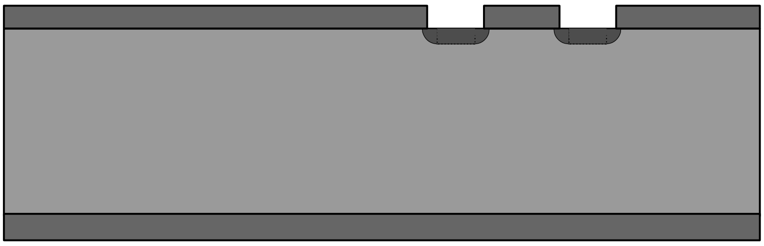

(*d*) HF dip etch of 30 nm thermal SiO_2 layer

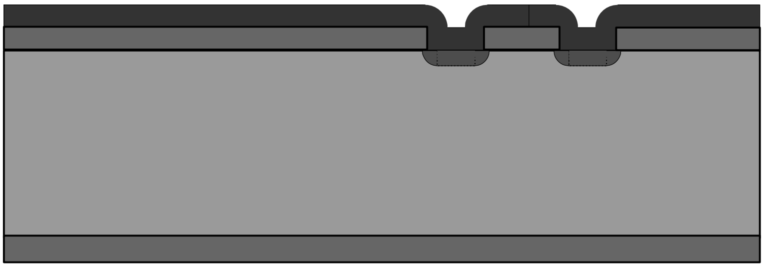

(*e*) A 1.475 μm Al sputter-deposited layer

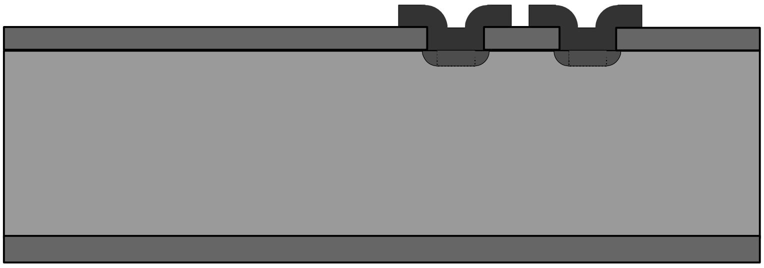

(*f*) Al contact pads after wet etching

Figure 4. 2: Process steps of heater fabrication

After that, a 2.5 µm thick PECVD silicon oxide layer was deposited on the top side to protect the aluminium contact pads from the damages that can potentially occur in the further processing steps. Another 2.5 µm thick PECVD oxide layer was deposited on the bottom side to serve as a mask during etching of the structures (figure 4.3a). The inlet, outlet, divider and collector manifolds and channels were processed in two-step DRIE process [13]. First, the inlet and outlet were etched 175 µm deep (figure 4.3b) by using the MASK IO and the remaining 100 µm were etched together with the 100 µm deep divider manifold, collector manifold and channels (figure 4.3c) by using the MASK CH, A close-up SEM image of the etched channels is shown in figure 4.4.

For bottom wafer, after etching alignment masks, a 2.5 µm thick SiO_2 was deposited on the top side by PECVD to serve as a mask for etching inlet and outlet 275 µm deep, by using the MASK IO. Another 6 µm thick SiO_2 was deposited on the bottom side by PECVD, which serves as electrical insulation of the devices during testing (figure 4.3d).

Before wafer bonding, the SiO_2 on the bottom side of the top wafer and on the top side of the bottom wafer was stripped by wet etching in BHF (1 : 7). Wafers were then cleaned by regular procedure in HNO_3, but also in RCA SC-1 solution (NH_4OH : H_2O_2 : H_2O = 1 : 1 : 5). RCA SC-1 solution removes particles in a superior way and also performs needed passivation of the bonding surface.

Two wafers were aligned in the contact aligner and bonding was performed at 400 ºC for 2 hours.. Finally, the protection SiO_2 layer on aluminium contact pads was removed by wet etching. Figure 4.5 gives the infrared image of bonded wafers, which shows that the wafers are nicely bonded (there is only one void). The aluminium contact pads and even the device structures can be seen

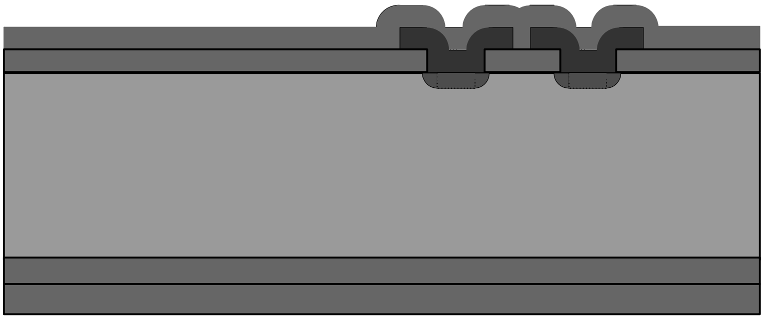

(*a*) 2.5 µm SiO_2 PECVD layers on both sides of top wafer

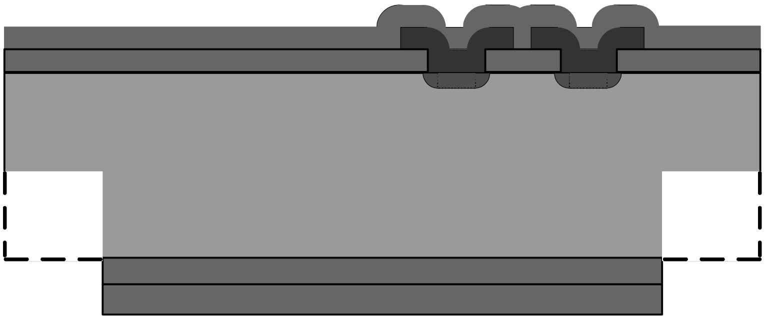

(*b*) 175 µm DRIE of inlet and outlet

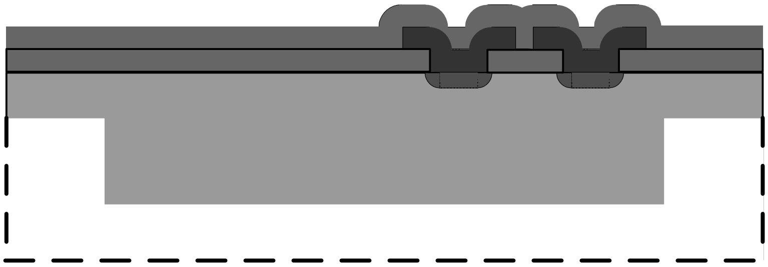

(*c*) 100 µm DRIE of inlet, outlet, divider manifold, collector manifold and channel structure

(*d*) PECVD of 2.5 µm on top side, 275 µm DRIE of inlet and outlet,
and PECVD of 6 µm on bottom side on bottom wafer

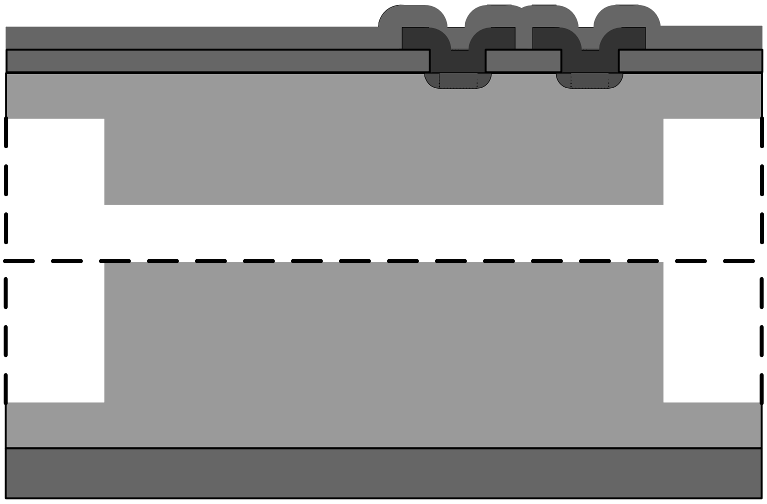

(*e*) Stripping of oxide on the bonding surfaces and direct wafer-to-wafer bonding

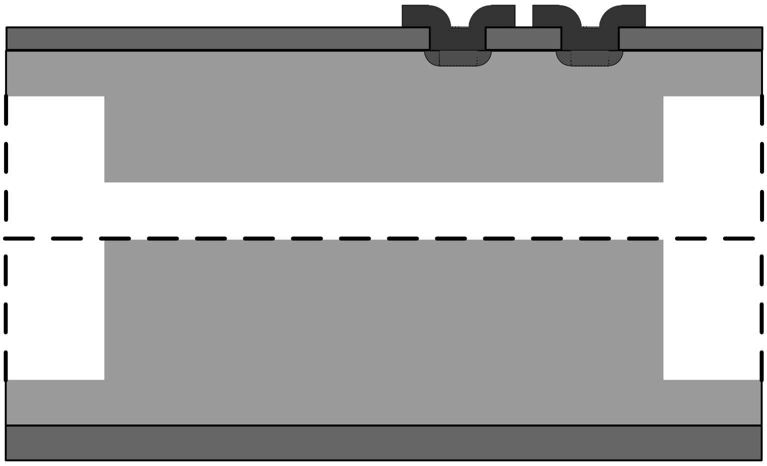

(*f*) Stripping of oxide protection layer on the Al contact pads

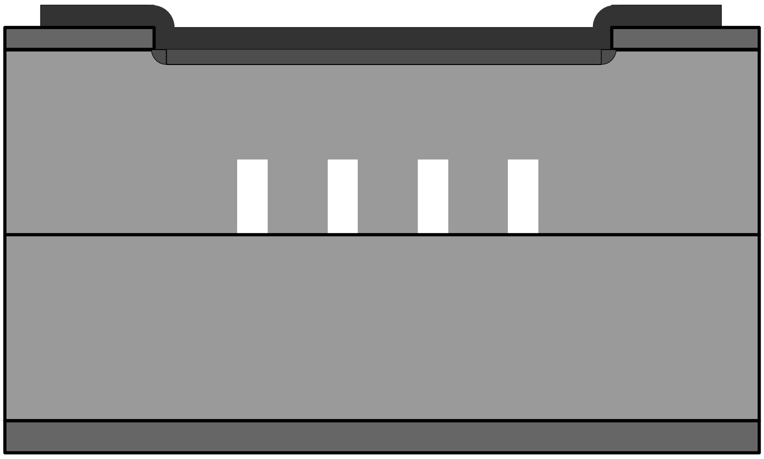

(*g*) Bonded wafers in different cross-section

Figure 4. 3: Process steps of channel patterning and wafer bonding

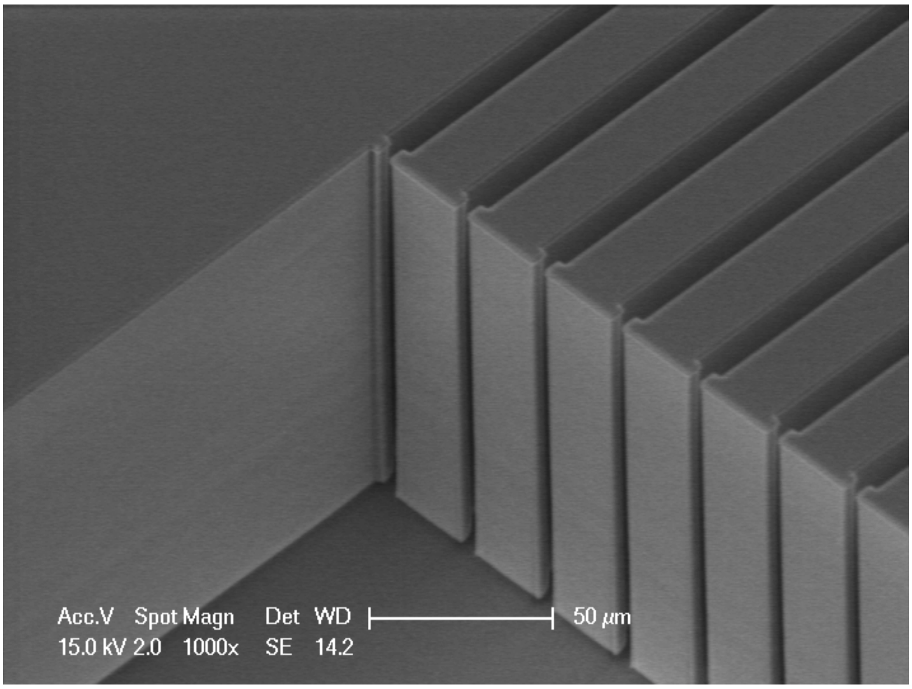

(*a*) SEM image of 10 μm wide straight channels

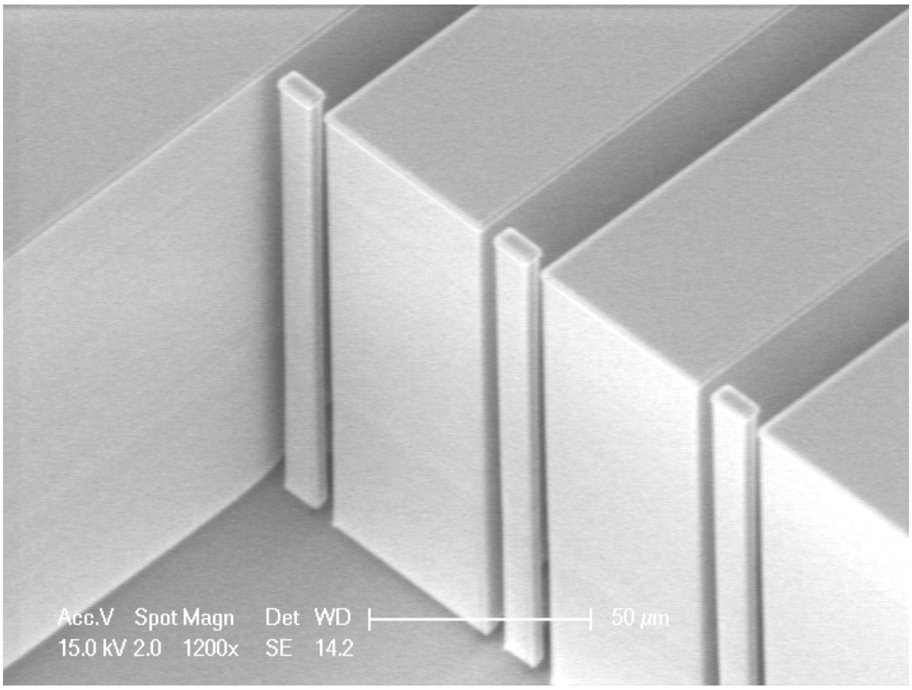

(*b*) SEM image of 20 μm wide straight channels

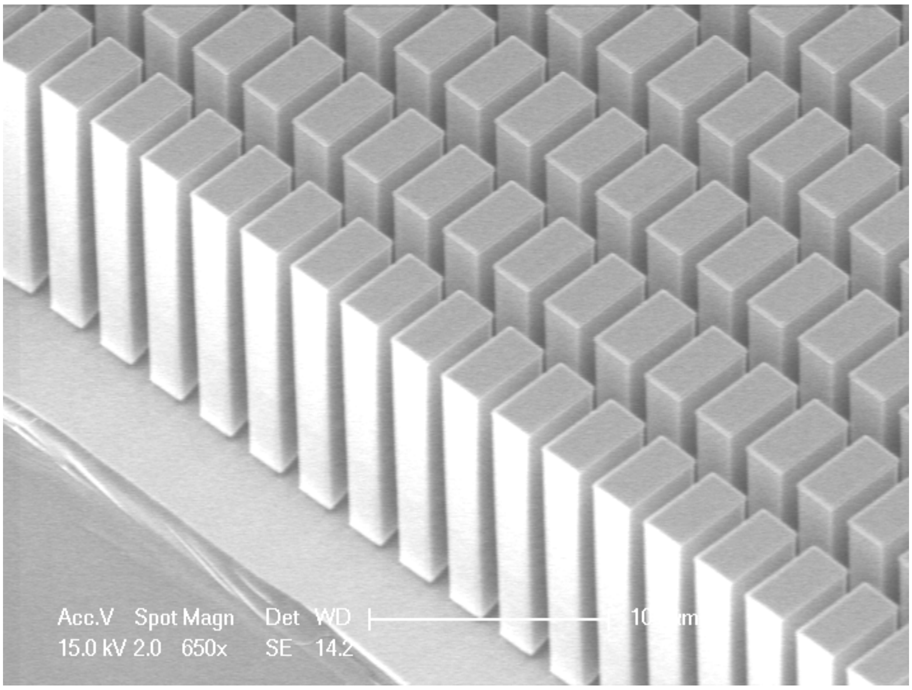

(*c*) SEM image of 10 μm wide crosslinked channels

Figure 4. 4: SEM images of three different etched channel structures

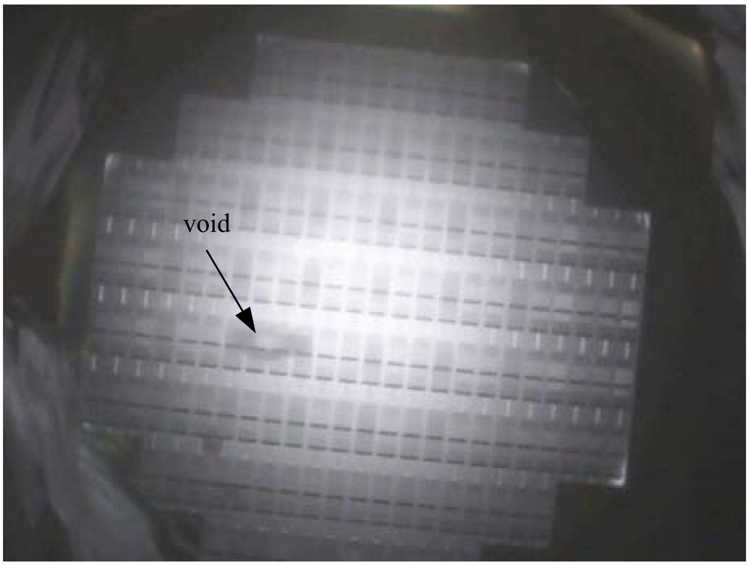

Figure 4. 5: Infrared image of bonded wafers

4.3 Device Dicing, Device Gluing, and Wire Bonding

The bonded wafers are shown in figure 4.6. In order to do the test or encapsulation, the whole wafer needed to be diced. Figure 4.7 shows the devices after dicing. As mentioned in Chapter 3, PCBs were needed for the test. The diced devices were glued to the PCBs with special glue, which was made by mixing two types of glue ARALDITE AV 138M and HARDENER HV 998 in the proportion 5 : 2. The inlet needles were also glued to the devices. These needles were manufactured by EFD company with a type 5125-B, which had an outer diameter ranging from 0.51 mm to 0.52 mm and an inner diameter ranging from 0.24 mm to 0.28 mm (figure 4.9).

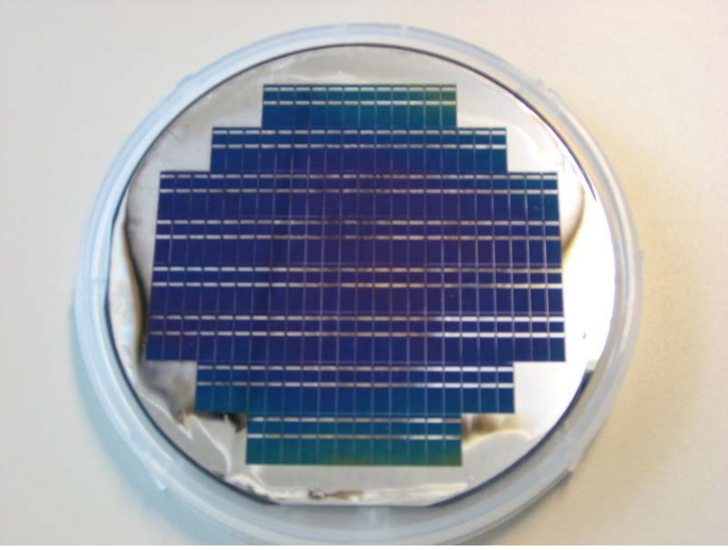

Figure 4. 6: Fully processed and bonded wafers

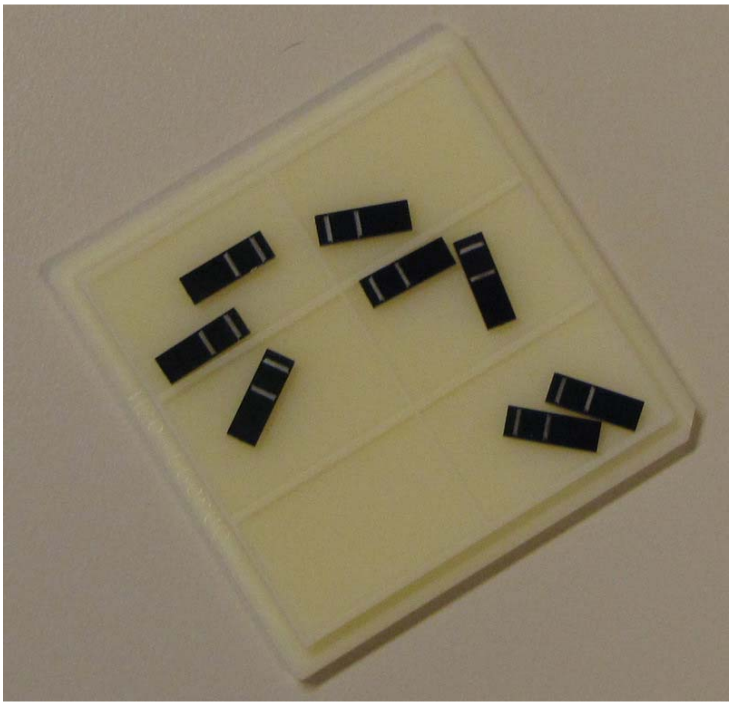

Figure 4. 7: Devices after wafer dicing

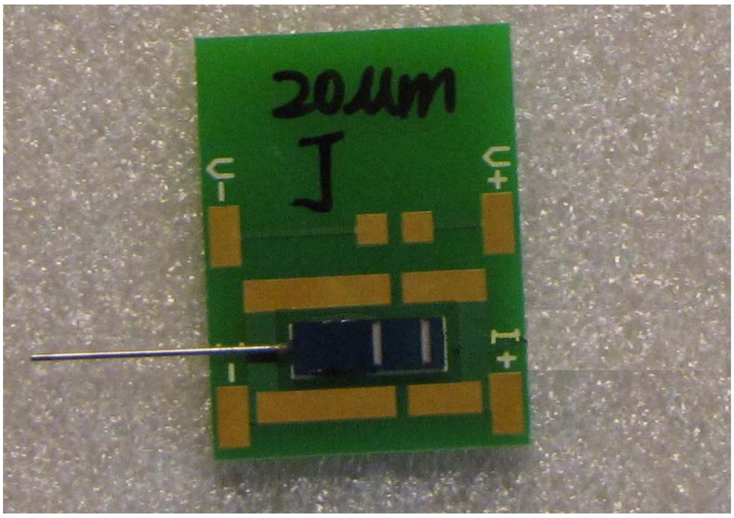

Figure 4. 8: Device after PCB and needle gluing

After gluing, wire bonding was performed with the aluminium wires, between the aluminium contact pads on the chip and the gold pads on PCB. Again, the maximum current density needed to be considered here. Aluminium wires were used for bonding, and the contact area between the aluminium wire and the aluminium pad on the device is a 125 μm × 50 μm rectangle. If we assume that only half of the perimeter of the contact area contributes to transport the current, the cross sectional area for transporting current of each bonding wire on the PCB is $(125 + 50) \times 1.48\ \mu\text{m}^2 = 259\ \mu\text{m}^2$, in which 1.48 μm is the thickness of the aluminium contact pads (figure 4.9). In Chapter 5, the measured resistance of the heater is given, which is from 74.65 Ω to 163.61 Ω in the interested temperature range. Therefore, the largest current to realize 20 W power would be about 0.52 A. We also know that the maximum current density in aluminium should be less than 1 mA/μm^2 [37]. Assuming the number of aluminium wires is N, then the following equation should be ensured:

$$(50+125)\times 1.48\ \mu\text{m}^2 \times 1\,\text{mA}\big/\text{mm}^2 \cdot N > 520\ \text{mA} \tag{4.1}$$

From the above equation, we have $N > 3$. For the current density on the gold pads on the PCB, we have the following equation:

$$(50+125)\times 0.3\ \ \mu\text{m}^2 \times 3.3\,\text{mA}\big/\text{um}^2 \cdot N > 520\ \ \text{mA} \tag{4.2}$$

In the above equation, 0.3 μm is the minimum thickness gold and 3.3 mA/μm^2 is the maximum current density in gold [38]. Then we have $N > 4$. In our design, five bonding wires were used. And another two bonding wires were used for measuring the voltage over the heater (figure 4.10).

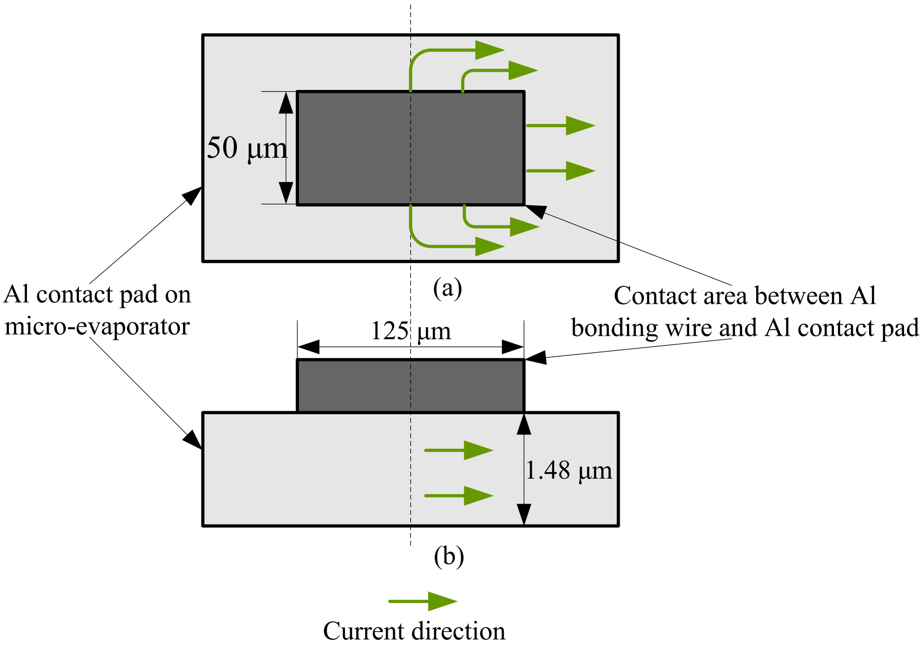

Figure 4. 9: Contact area and current direction
between Al bonding wires and Al pads on micro-evaporator

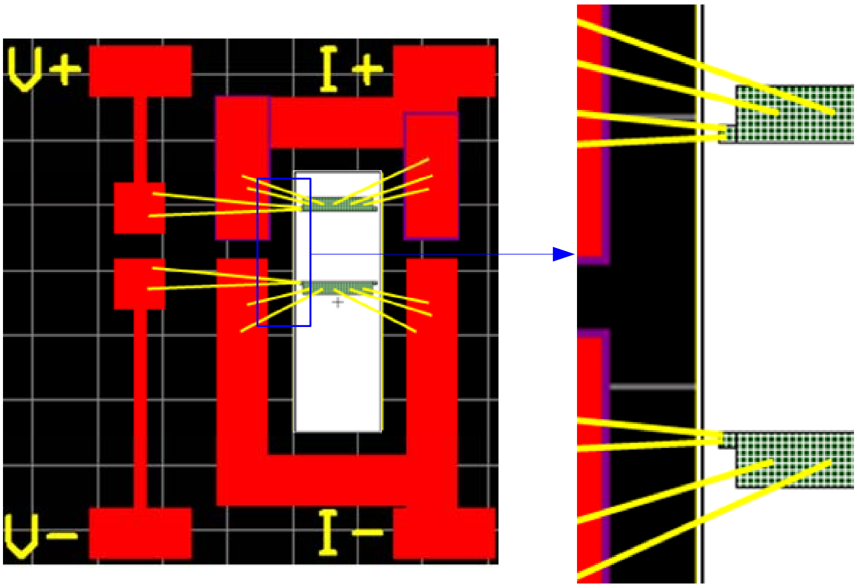

Figure 4. 10: Schematic of wire bonding and the zoom-in part

4.4 Conclusions

Fabrication of the micro-evaporators was presented. It consisted of three main steps, fabrication of the heater, channel structure patterning and direct wafer-to-wafer bonding. The channels structures were patterned in two steps to avoid the thin wall between the inlet/outlet and the divider/collector manifolds.

After wafer bonding, the bonded wafers were diced in to devices. And inlet needles were glued into the inlets, and then the devices were glued onto the PCBs. Wire bonding was done to make electrical connections between the aluminium pads on the devices and the gold pads on the PCBs. In this process, the electromigration in both materials needed to be considered.

Chapter 5

Measurement of Micro-Evaporator

5.1 Introduction

In this chapter, heater characterization and fluidic measurement are introduced. The heater characterization was performed in the measurement room of ECTM, DIMES, and the fluidic measurement was carried out in the measurement lab of TNO. The test result of heater characterization proved that the heater could function properly and supply enough power. And the test results of the fluidic measurements supplied meaningful clues for the future work.

5.2 Heater Characterization

5.2.1 Measurement Set-up

As mentioned in Chapter 3, the heater has two functions: one is to mimic the processes cause heating; the other one is to serve as a temperature sensor to monitor the temperature of the device. In order to measure and control the temperature of the heater accurately, it is of great importance to know the temperature dependence of the resistance of silicon. The characterization of the heater was performed before dicing the wafer (figure 4.6) and carried out in the measurement room of ECTM. The characterization was performed in a microchamber probe station (Cascade Microtech, model: summit 12971B) (figure 5.1), the temperature of which was control by thermochuck (Temptronic, model: TP0315B-2) (figure 5.2). The input current and output voltage signals were forced and measured by an 8 slot precision measurement mainframe (Agilent E5270B) (figure 5.3).

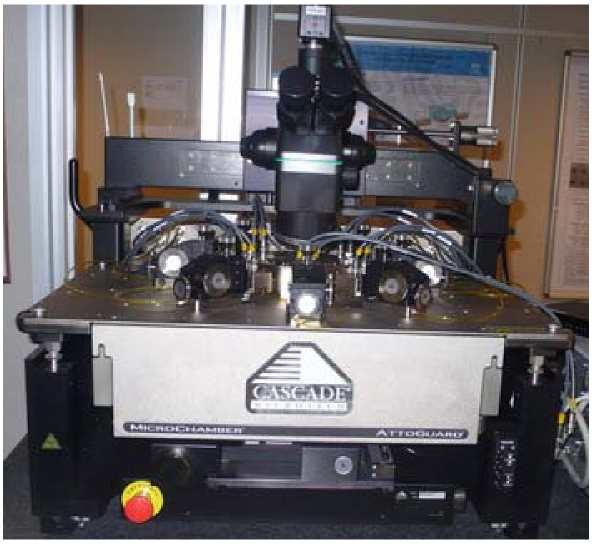

(*a*) Cascade probe station

(*b*) Control facility of the probe station

Figure 5. 1: Cascade microchamber probe station

(*a*) Thermochuck programme interface

(*b*) Temperature control facility

Figure 5. 2: Thermochuck

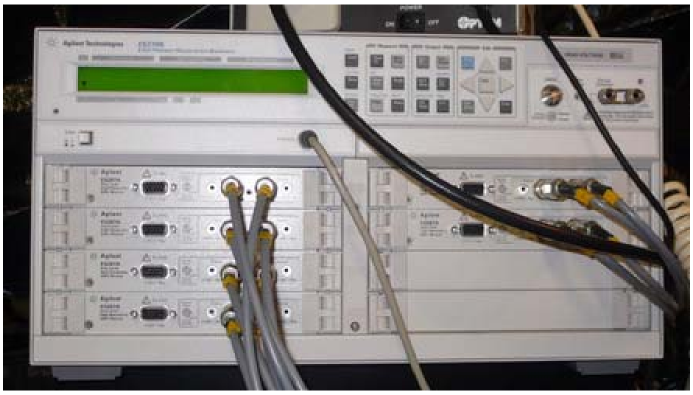

Figure 5. 3: Agilent 8 slot precision measurement mainframe

5.2.2 Measurement Procedures

The resistance of the heaters on three different devices was measured by using four-point probe method [39] in a temperature range from 30 ºC to 160 ºC. Figure 5.4 gives the schematic of two-point probe method and four-point probe method. A current source supplies the current, I, through the resistor of the resistance, R. The voltage, V, over the resistor is measured by a voltmeter. As a result, the resistance, R, can be expressed as:

$$R = \frac{V}{I} \tag{5.1}$$

For two-point probe method, the resistance would be $R + 2 \cdot R_{con}$ instead of R. R_{con} is the resistance of the connection wires, which would cause an error of the measured resistance. The resistance of the connection wires with the voltmeter is R_{conv}, which can be ignored because the current goes through the voltmeter is very small due to the high resistance of the voltmeter.

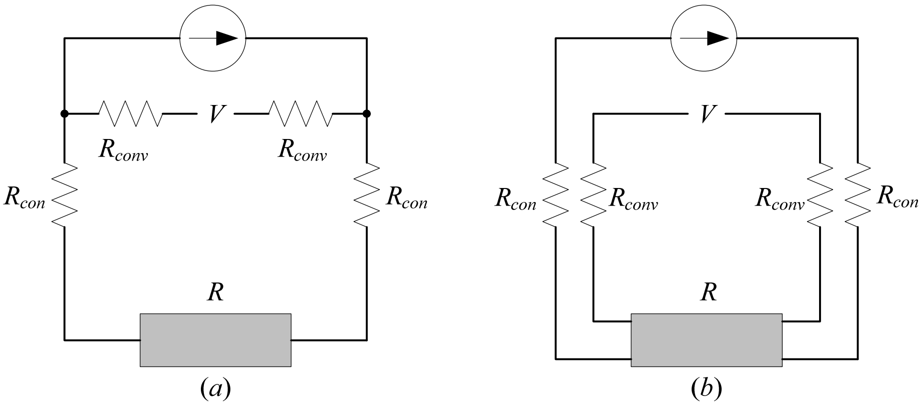

Figure 5. 4 Schematic of
(*a*) two-point probe method and
(*b*) four-point probe method

Figure 5.5 shows the schematic of the set-up for characterizing the resistance of the heater. There were six probes, but for this characterization only four probes were used. Probe 1 and probe 3 were used to supply the current through the heater, whilst probe 4 and probe 6 measured the voltage drop across the heater. In order to make sure that the current was going evenly though the heater, probe 1 and probe 3 were placed in the middle of the side edge of the aluminium contact pads, as shown in figure 5.5.

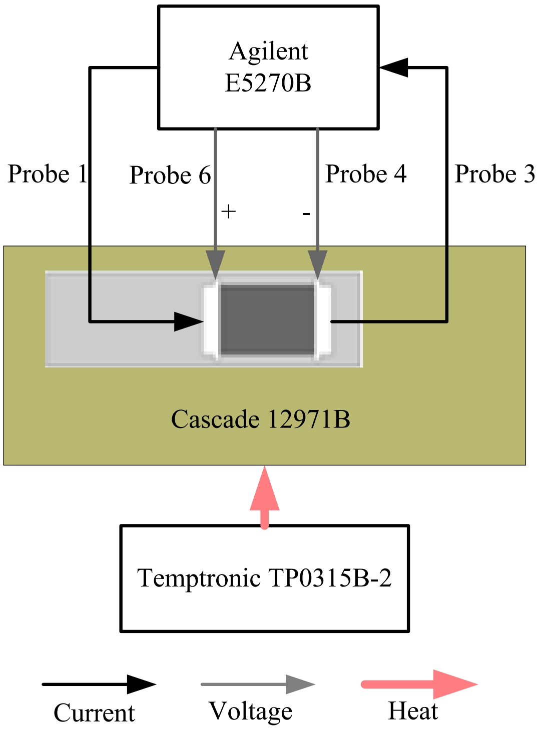

Figure 5. 5: Schematic of heater characterization

5.2.3 Measurement Results

The heater characterization was performed on all three devices in the temperature range from 30 ºC to 160 ºC. The mean value of the resistance at each temperature was calculated and was regarded as the exact value of the resistance at that temperature (table 5.1).

Resistance (Ω) / Temperature (ºC)	Devices of type A	Devices of type B	Devices of type C	Mean value
30 ºC	74.25	74.35	75.36	74.65
40 ºC	79.91	80.04	81.15	80.37
50 ºC	85.80	85.94	87.13	86.29
60 ºC	91.90	92.04	93.34	92.43
70 ºC	98.22	98.33	99.76	98.77
80 ºC	104.73	104.84	106.38	105.32

85 ºC	108.03	108.19	109.77	108.67
90 ºC	111.39	111.58	113.22	112.06
95 ºC	114.79	114.95	116.68	115.47
100 ºC	118.28	118.42	120.21	118.97
105 ºC	121.80	121.92	123.79	122.50
110 ºC	125.27	125.38	127.33	125.99
115 ºC	128.85	128.97	130.98	129.60
120 ºC	132.43	132.58	134.68	133.23
125 ºC	136.07	136.21	138.39	136.88
130 ºC	139.75	139.92	142.17	140.61
135 ºC	143.53	143.67	146.02	144.41
140 ºC	147.25	147.37	149.81	148.14
150 ºC	154.86	154.98	157.56	155.80
160 ºC	162.55	162.73	165.54	163.61

Table 5. 1 Measured resistance and mean value on three devices

The test data was processed with MATLAB software. The second order fitted resistance and temperature dependence curve is shown in figure 5.6a, which can be expressed as the function: $R = 9 \times 10^{-4} \cdot T^2 + 5.2 \times 10^{-1} \cdot T + 58.1$. However, as mentioned before, the heater should also work as a sensor to monitor the temperature of the device. Therefore, the temperature is expressed as a function of resistance, which is $T = -2.6 \times 10^{-3} \cdot R^2 + 2.1 \cdot R - 110$ (figure 5.6b). In the former two equations, the unit of R is Ω and the unit of T is ºC. In this resistance range, a 20 W power can be supplied by a voltage source have a 60 V maximum output.

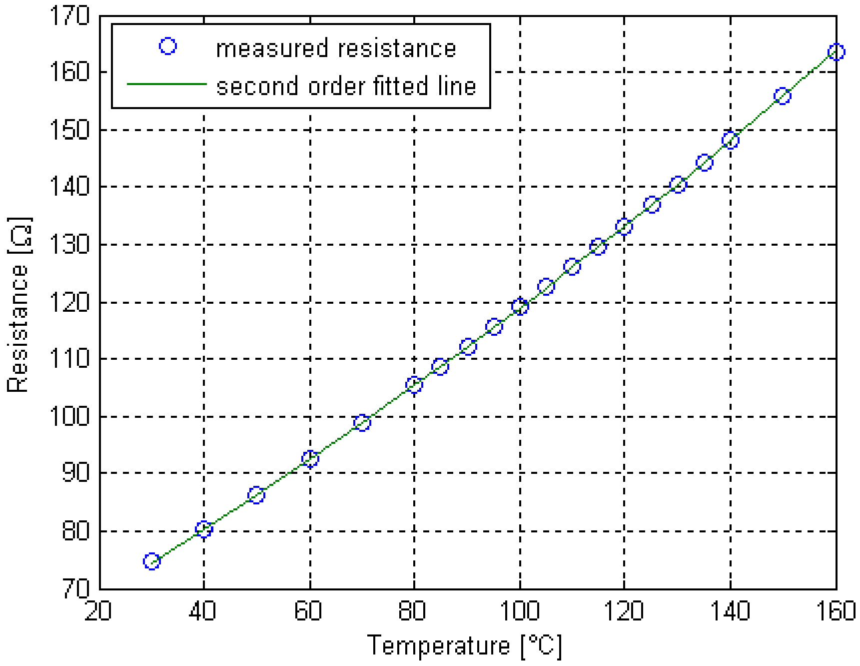

(*a*) Resistance as a function of temperature

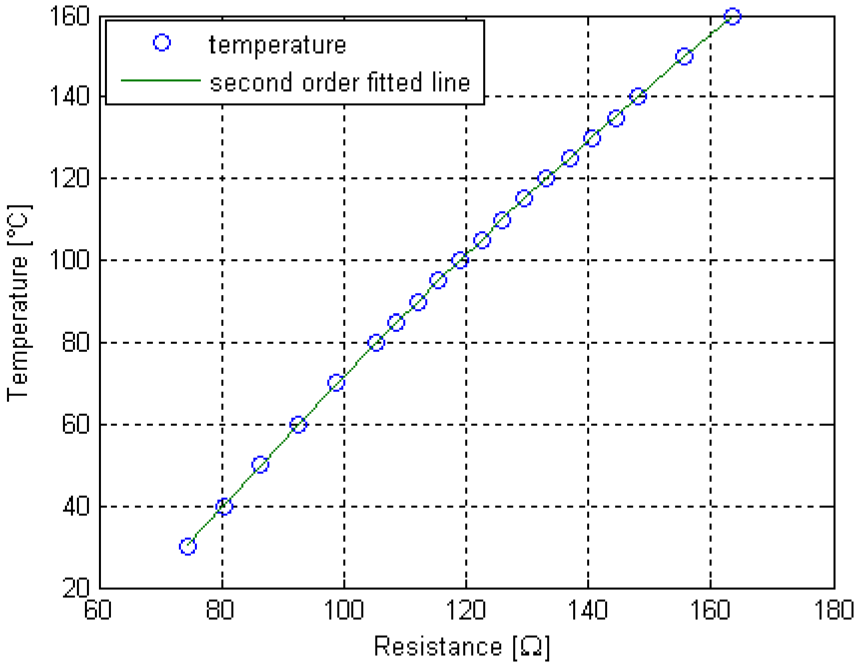

(*b*) Temperature as a function of resistance

Figure 5. 6: Temperature dependence of the electrical resistance of the heater

5.3 Fluidic Measurements

5.3.1 Measurement Set-up

The fluidic measurements were performed in the measurement lab of TNO. Figure 5.7 shows the schematic of the fluidic measurements. The photo of the measurement set-up is given in figure 5.8. For the electrical measurements with the sustained flow, an electrical source HP E3631A was used as a voltage supply; the current through the heater was measured by KEITHLEY 2700 multimeter; and the voltage across the heater was read by FLUKE 8840A multimeter. A PID controller was used to keep the temperature of the device at the constant value. The flow rate was supplied by a syringe and a precise programmable syringe pump AL1000. Figure 5.9 gives the close-up photo of the device being tested.

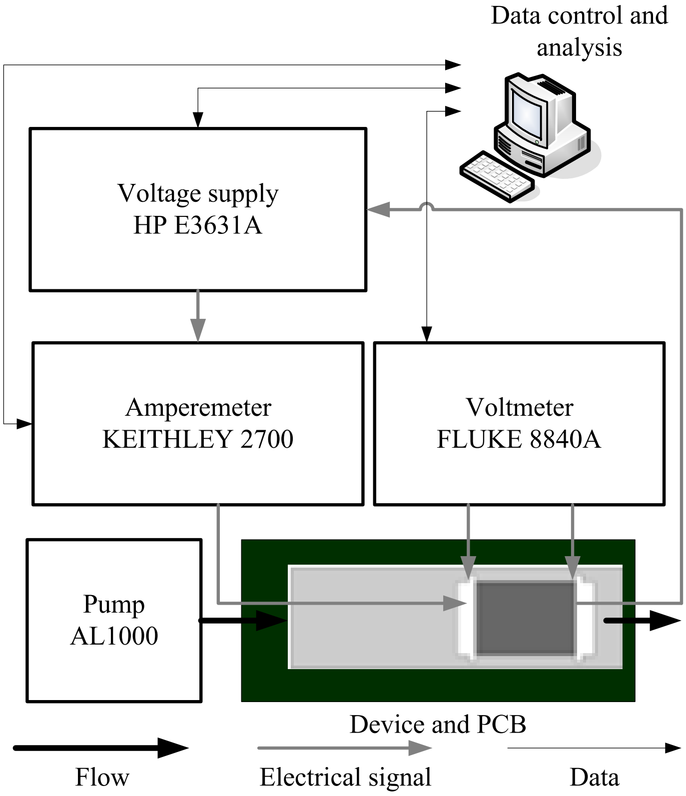

Figure 5. 7: Schematic of fluidic measurements

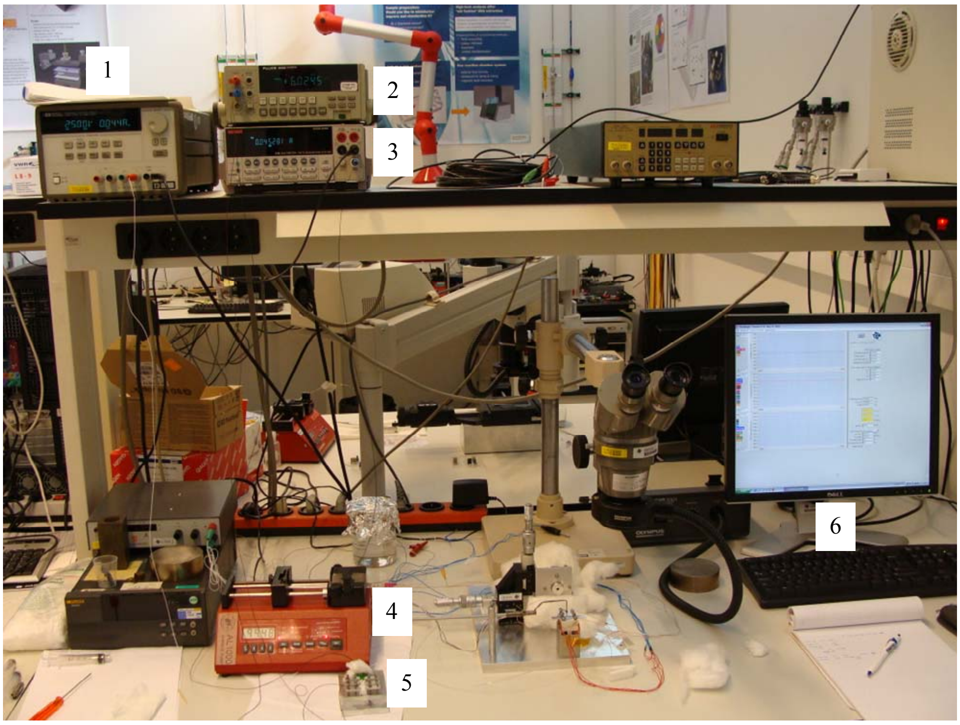

1. HP E3631A, 2. FLUKE 8840A, 3. KEITHLEY 2700,
4. Syringe and Syringe Pump AL1000, 5. Micro-evaporator, 6. PC with PID Controller

Figure 5. 8: Photo of fluidic measurement set-up

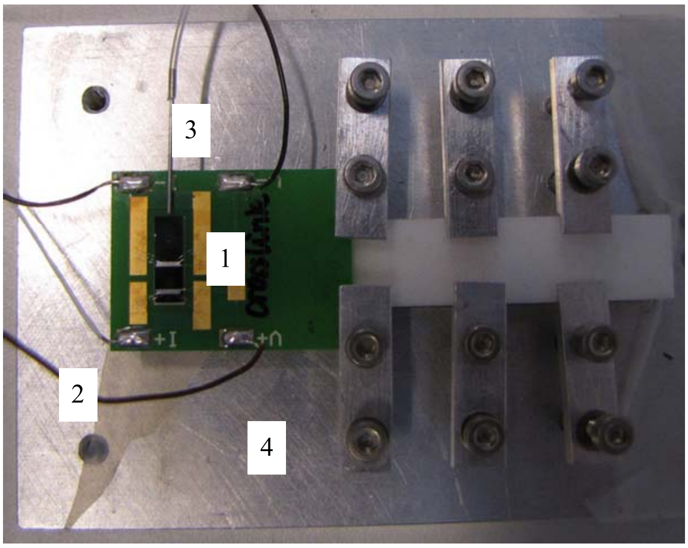

1. Device on PCB, 2. Soldered wires,
3. mounted needle and tube, 4. PCB holder

Figure 5. 9: Close-up photo of the device being tested

5.3.2 Measurement Procedures

The main purpose of this measurement is to find the highest fully evaporated flow rate of each type of devices, from which the power absorption of the flow, heat fluxes, and heat coefficients can be derived. But before testing this, there are some other parameters that needed to be verified. The first parameter is the stability of the PID controller. As mentioned before, the PID controller was used to keep the temperature of the devices at a constant value during the test. So the stability or the ability to avoid big oscillation in temperature is a very important performance of a PID controller. Another parameter that needs to be known is the heat loss of the devices to the ambient, which is due to the convective heat transfer from the device to the air and the conductive heat transfer from the device to the PCB and other connections.

Stability of the PID Controller

The stability of the PID controller at 120 ºC on device 2 (type B) is given in figure 5.10, which shows that when the demineralized water flow rate is from 0.02 ml/h to 30 ml/h, the standard deviation of the temperature profile at 120 ºC is 1.31 ºC. However, in the interested flow rate range from 0.02 ml/h to 1 ml/h, the standard deviation of temperature profile is 1.46 ºC, because of the influence of boiling. And in the flow rate range from 1 ml/h to 30 ml/h, the standard deviation of temperature profile is 0.58 ºC. The PID controller has a good stability.

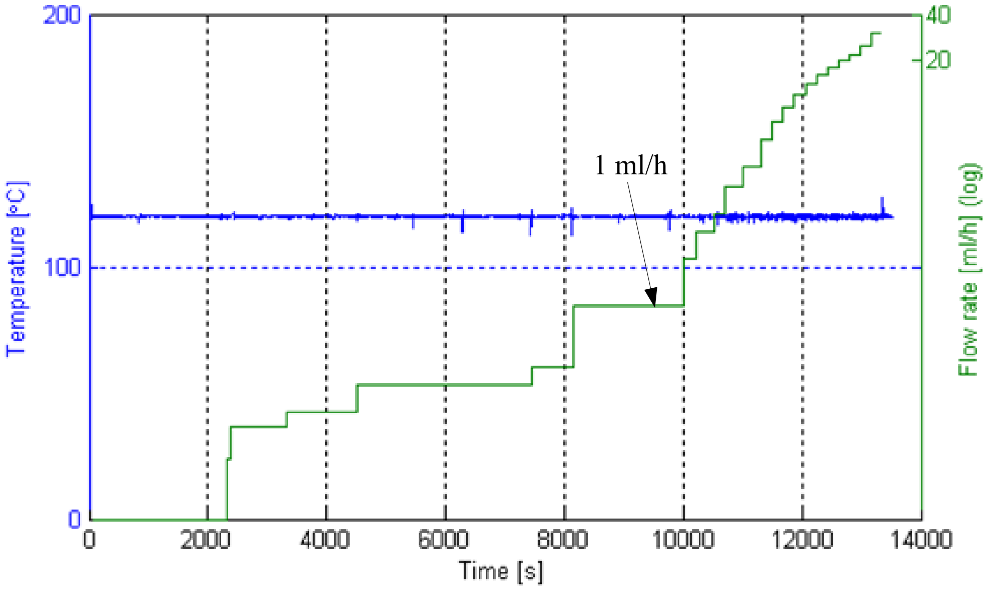

Figure 5. 10: Temperature profile of 120 ºC at flow rate up to 30 ml/h

Heat Losses of the Micro-Evaporators

The testing of heat losses was performed on three different channel structured devices. The devices were heated from 70 ºC to 160 ºC without any flow through the channels, and then the dissipated power could be tested. Heat losses originated from two types of heat transfer: convective heat transfer to the ambient air and conductive heat transfer to the PCB holding the devices. The testing was performed on device 1, device 2, and device3, which were picked up from the devices of type A, type B, and type C. Figure 5.11 gives the test results of three different devices, respectively. And the exact values are given in table 5.2. The test results for each device can also be fitted with a first order line (to show its linearity), for each device which are $P = 4.7 \times 10^{-3} \cdot T - 0.3114$, $P = 4.5 \times 10^{-3} \cdot T - 0.3078$, and $P = 4.4 \times 10^{-3} \cdot T - 0.3050$, respectively.

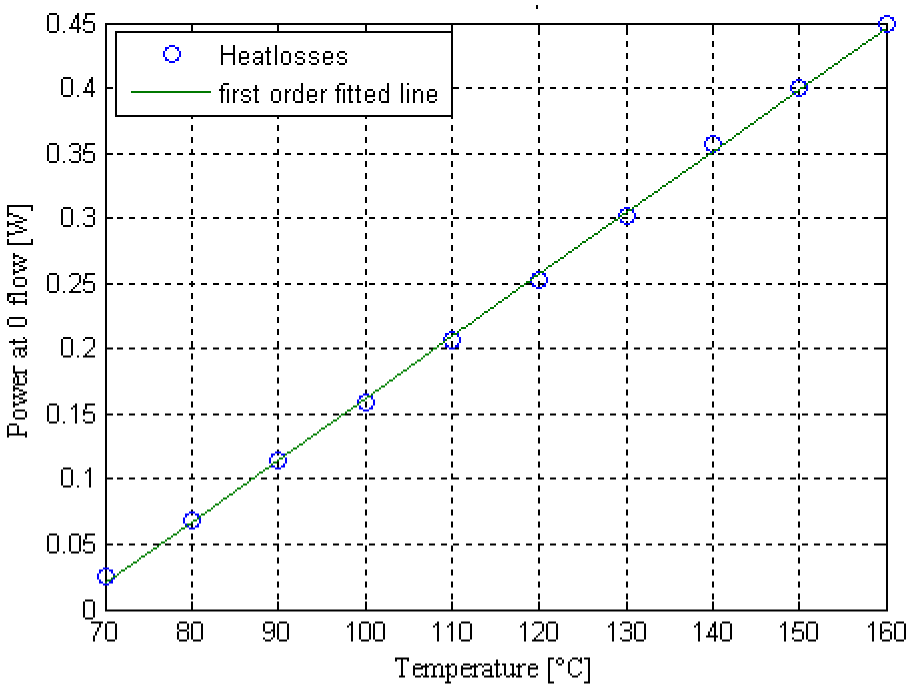

(*a*) Heat losses of device 1 (type A)

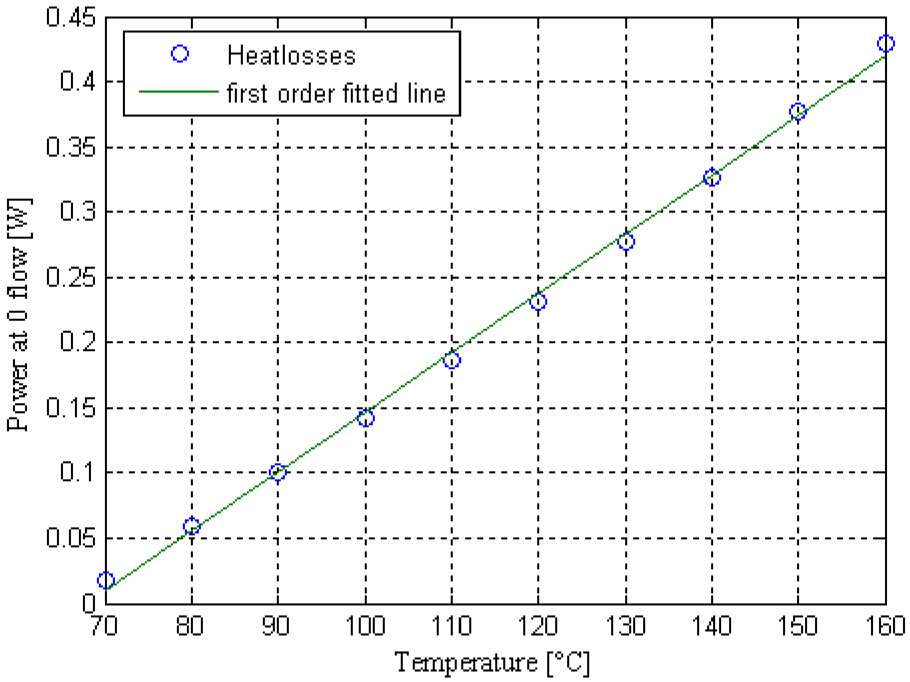

(*b*) Heat losses of device 2 (type B)

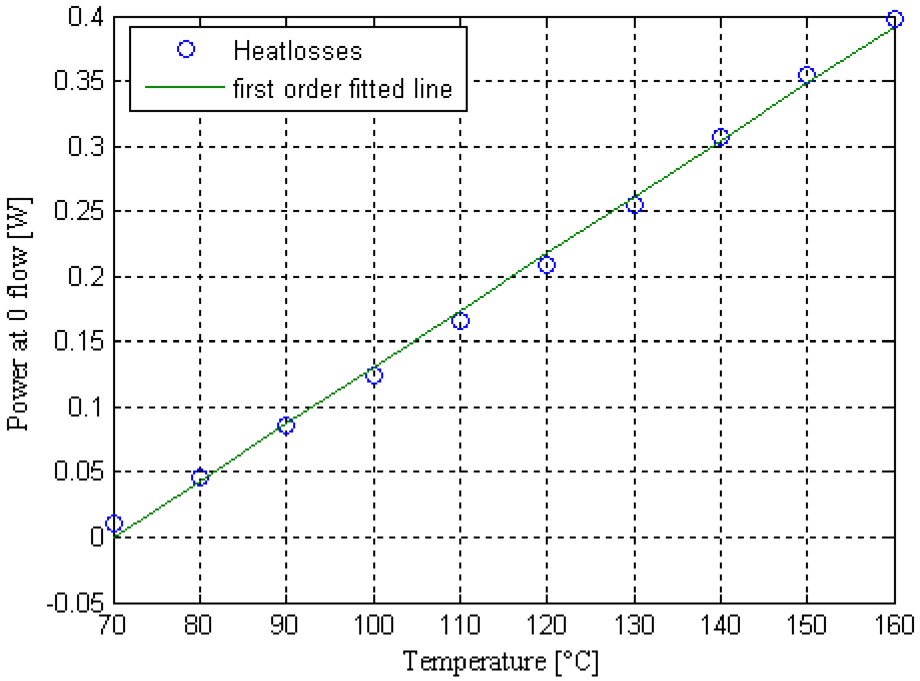

(*c*) Heat losses of device 3 (type C)

Figure 5. 11: Heat losses from 70 ºC to 160 ºC

Heat losses (W) / Temperature (ºC)	Device 1 (type A)	Device 2 (type B)	Device 3 (type C)
70	0.0255	0.018	0.0102
80	0.068	0.0597	0.046
90	0.114	0.1013	0.0861
100	0.1595	0.1426	0.1246
110	0.2066	0.1863	0.1665
120	0.2526	0.2305	0.2089
130	0.3016	0.2765	0.2542
140	0.3565	0.3271	0.3075
150	0.3995	0.3769	0.3543
160	0.4487	0.4295	0.3974

Table 5. 2: Heat losses from 70 ºC to 160 ºC

Fully Evaporated Flow Rate

The last step of the testing was to get the fully evaporated flow rate of each device. In order to avoid pre-mature boiling, before testing, the water was boiled in a beaker on a hot-plate for about 5 minutes to get rid of the air dissolved in the water. The test procedure was to keep the flow rate at constant values, and then to increase the temperature of the heater from 80 ºC to 160 ºC. The power consumption at these temperatures was the sum of the heat losses and the heat absorption by the water flow for evaporation.

Absorbed heat was heating the wafer flow from 20 ºC (room temperature) to 100 ºC and changing the phase of water from liquid to vapour. Based on equation 3.17, power needed for the fully evaporation of water flow rate of 1 ml/h (including heating from the room temperature) can be calculated as 0.72 W.

Figure 5.12 shows the power absorption at different flow rates from 80 ºC to 160 ºC on three devices. It is the total power consumption minus heat losses, which is the power only absorbed by the water flow. As shown in figure 4.8, there is no needle glued at the outlet of the device. When the temperature is lower than 100 ºC, the water goes out of the device from the outlet could gather on the PCB. As temperature increases, this amount of water can also be vaporized, but absorbs extra power. Therefore the total power would be higher than the power for heating and vaporizing the water flow in the channels, see the peaks in figure 5.12a. However, after this amount of water is evaporated, the power absorption drops and equal to the power only for fully evaporating the flow in the channels.

The curves in figure 5.12a show the power absorption of different water flow in device 1 (type A). Taking the curve at 0.1 ml/h flow rate as an example, the curve can be divided into three parts according to the temperature range and be analyzed respectively. When the temperature is lower than 100 ºC, the heat is mainly absorbed by single-phase flow. From 100 ºC to 110 ºC, boiling occurs, so there is two-phase flow in the device. There is a peak at 110 ºC, as explained in the previous paragraph. From 120 ºC to 160 ºC, the power absorption at these temperature is about 0.7 W, because the water gathered on the PCB was all evaporated and the water flow in the device was also fully evaporated, which can be proved by the calculated value before. When the flow rate is 0.2 ml/h, the test result can be explained in the same way as 0.1 ml/h flow rate. The power absorption peak appears at 130 ºC. When the temperature is higher than 130 ºC, the power absorption lowers to about 0.14 W, which means 0.2 ml/h flow rate can also be fully evaporated. As the flow rate further increases, it is impossible to be completely evaporated. Therefore, the power absorbed by 0.3 ml/h flow rate at 150 ºC and 160 ºC is about 0.18 W instead of 0.21 W. This situation can be explained in three different ways: first, the device itself is not able to evaporate more water; second, boiling happens in the divider manifold or even in the inlet, which blocks the water flow; third, as mentioned in Chapter 2, explosive boiling occurs in sub-50 μm diameter channels, which probably pushes the water in front of the bubble out of the device. This amount of water does not consume power. Thus, a conclusion that the device can fully evaporate a flow rate between 0.2 ml/h and 0.3 ml/h can be drawn.

The same method can be used to analyze figure 5.12b and figure 5.12c. Figure 5.12b shows that device 2 (type B) can fully evaporate a flow rate between 0.3 ml/h and 0.4 ml/h. Figure 5.12c shows the flow rate that can be completely evaporated by device 3 (type C) is between 0.6 ml/h and 0.7 ml/h. Therefore, devices of type C have the best performance among the three different structured devices.

According the above test results, the heat fluxes and heat transfer coefficients on the three devices can also be derived. These values can be calculated at 130 ºC, because for pool boiling the critical heat flux appears at about 125 ºC, but for flow boiling the critical heat flux should appear at higher temperatures as shown in figure 2.13. For device 1and device 2, the fully evaporated flow rates at 130 ºC are both about 0.2 ml/h, which result in a heat flux of 19.2 kW/m^2 and a heat transfer coefficient of 0.64 kW/m^2·K. For device 3, at 130 ºC the fully evaporated flow rate is about 0.3 ml/h, which leads to a heat flux of 29 kW/m^2 and a heat transfer coefficient of 0.96 kW/m^2·K.

Because the heater characterization was performed on the wafer level (figure 4.6), the tested resistances at different temperatures were influenced by the cross-talk from the adjacent devices. Actually, after dicing the bonded wafers, mounting the inlet needle, gluing the device onto the PCB, and wire bonding, the real resistances of the heater at different temperatures were larger than the measured values during heater characterization, which resulted in that the real temperatures during the fluidic measurement were lower than the temperatures shown on figure 5.12. However, after wire bonding, it was difficult to do the heater characterization again. This correction will be done by the author in the future.

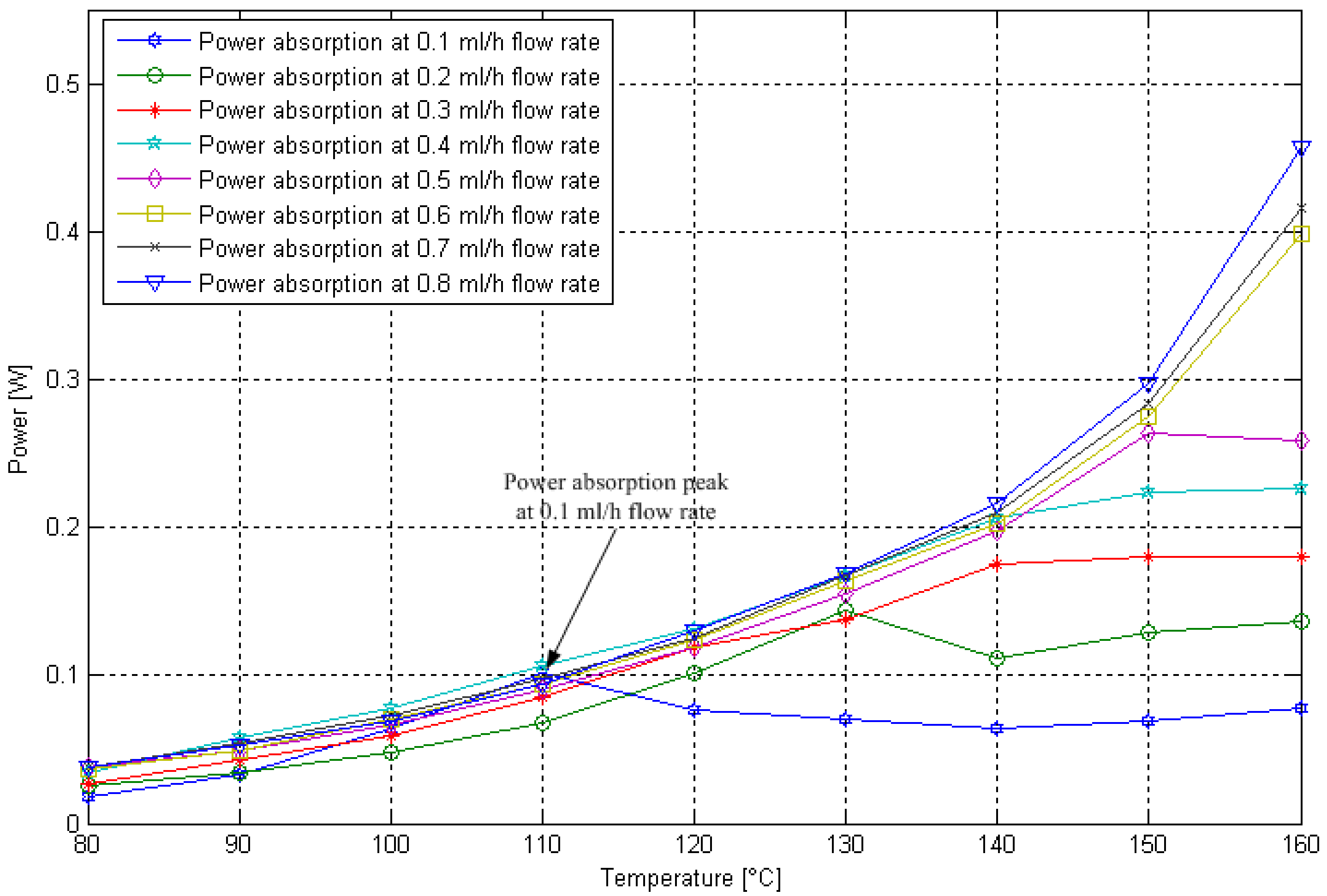

(*a*) Power absorption at different flow rates for device 1 of type A

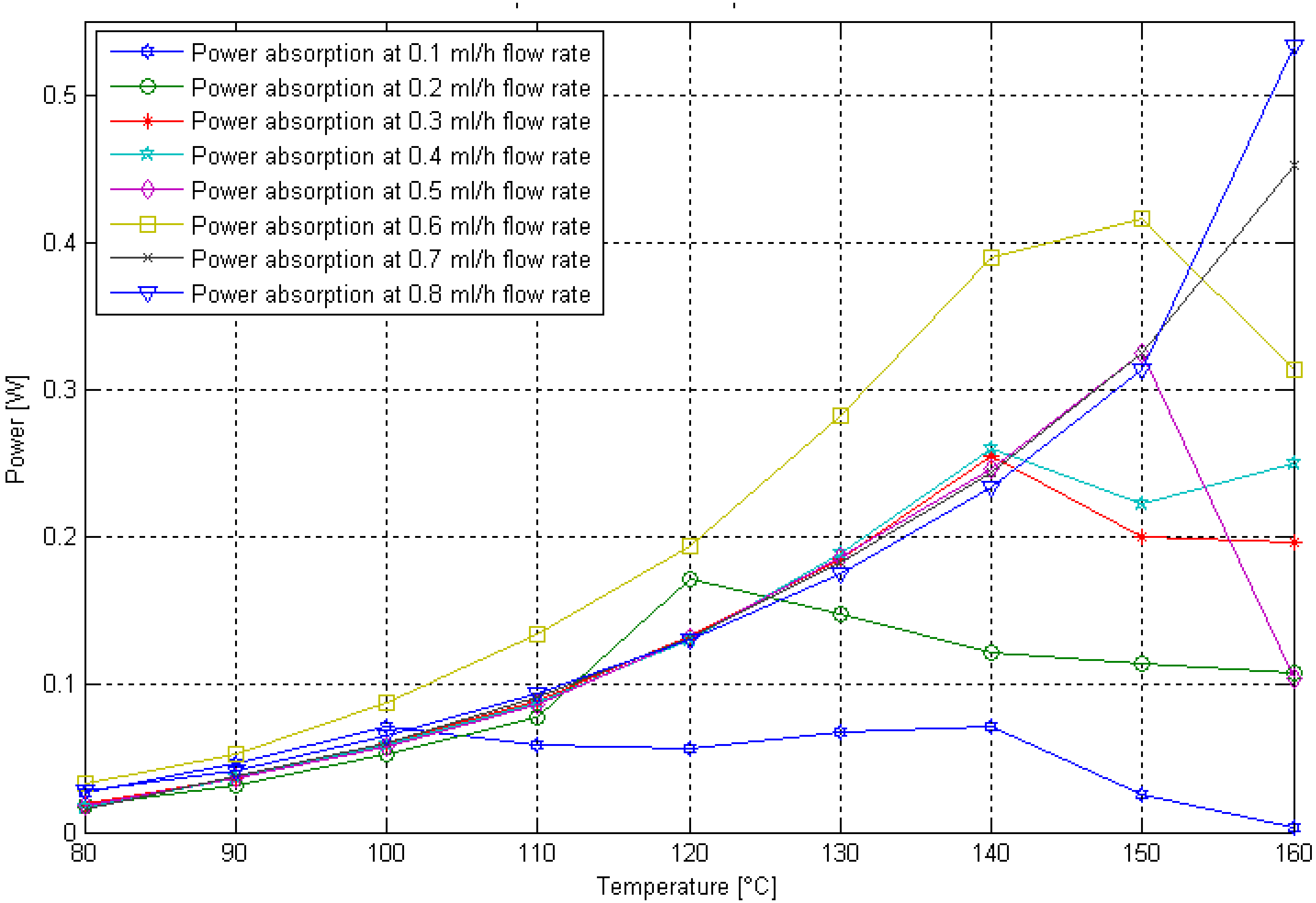

(*b*) Power absorption at different flow rates for device 2 of type B

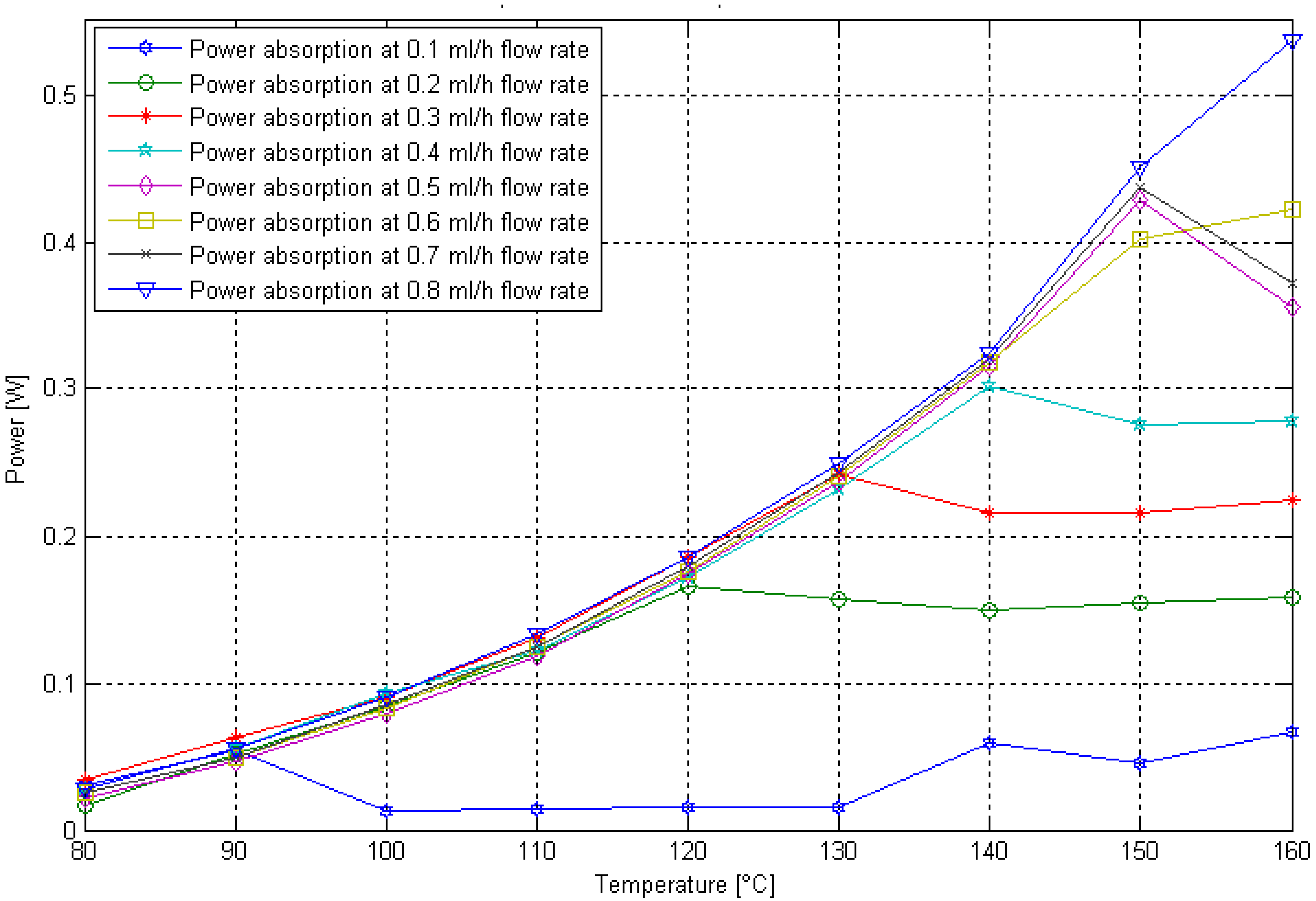

(*c*) Power absorption at different flow rates for device 3 of type C

Figure 5. 12: Power absorption at different flow rates, at temperatures from 80 ºC to 160 ºC

5.4 Conclusions

The measurements of the devices were discussed in this chapter, which consisted of two parts: the electrical measurement and the fluidic measurement. Heat characterization was performed first, because the temperature dependency was necessary for the heater to serve as a temperature sensor. In the fluidic measurement, the fully evaporated flow rates of three different devices were measured, from which the heat fluxes and heat transfer coefficients could be derived.

Chapter 6

Conclusions and Outlook

6.1 Conclusions

The design, fabrication, and measurement of the micro-evaporators have been investigated in this work. Various aspects of the problem have been addressed, ranging from the heat transfer background to the heat transfer enhancement by fin structure, and from the fabrication steps to the testing procedures. In the following, the main results from this work are summarized, followed by a set of recommendations for future study.

In Chapter 2, the heat transfer theory was introduced. First, three different modes of heat transfer were studied, which were conduction, convection and radiation. Second, the theory of pool boiling was discussed, in which different boiling regimes were introduced. Finally, basing on the pool boiling theory, flow boiling in conventional channels and micro-channels were explained. In sub-50 μm diameter channels, because of the small confined space, explosive boiling is dominant.

Chapter 3 focused on the design of the channel structure. First, the fin structure theory was introduced, which consisted of the effective height of the fin and the increase of heat transfer by using fin structure. Second, the design of the micro-evaporators with three different fin structures was discussed, which were 10 μm wide straight channel structure, 20 μm wide straight channel structure and 10 μm wide crosslinked channel structure. Third, the layout design of the devices was introduced, and four masks were presented. Finally, the schematic of the PCB was shown.

In chapter 4, we discussed the fabrication of the micro-evaporators. The major steps of fabrication of the devices and also the wire bonding of the devices to the PCB were introduced. In the wire bonding part, the maximum current density of aluminium bonding wires needed to be considered.

Chapter 5 gave the measurement of the micro-evaporators, which consisted of two parts: the characterization of the heater and fluidic measurements. The test results of heat characterization proved that the heater was able to realize enough power for evaporation. Whilst the test results of fluidic measurement showed that the three different structured devices worked properly and the device with 10 µm crosslinked channel structure had the best performance, although the fully evaporated flow rates of these devices were relatively low. The three causes for this problem were also discussed.

6.2 Recommendations for Future Work

6.2.1 Avoiding Boiling in Divider Manifold

As discussed in Chapter 5, there are three reasons that could explain why the micro-evaporators have difficulties to achieve higher fully evaporated flow rate. One of them is because of the high thermal conductivity of silicon, boiling could have already occurred at the divider manifold or even at the inlet of the device, which blocks the flow going into the channels and causes a lower flow rate or even zero flow rate. The solution to this problem is that the silicon above the divider manifold or even at the entrance of the channels can be etched partially to reduce the heat transferred to this area, which can avoid the boiling in the divider manifold and achieve a higher flow rate. However, a margin should be kept to ensure the strength of the device, as shown in figure 6.1.

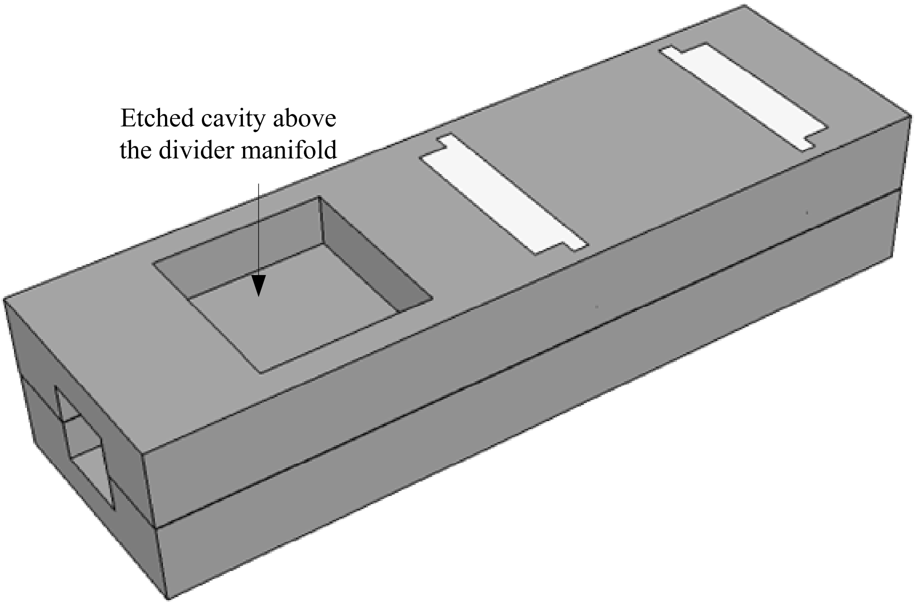

Figure 6. 1: Schematic of the etching silicon above the divider manifold

6.2.2 Other Pin Fin Channel Structures

In the thesis, three channel structures are investigated, which are 10 µm wide straight channels, 20 µm side straight channels, and 10 μm wide crosslinked channels. The test result has proved that the fully evaporated flow rate of the micro-evaporator with crosslinked channel structure is the highest. There are other crosslinked channel structures (pin fin shapes) that have been studied or applied, which could achieve better performances (figure 6.2).

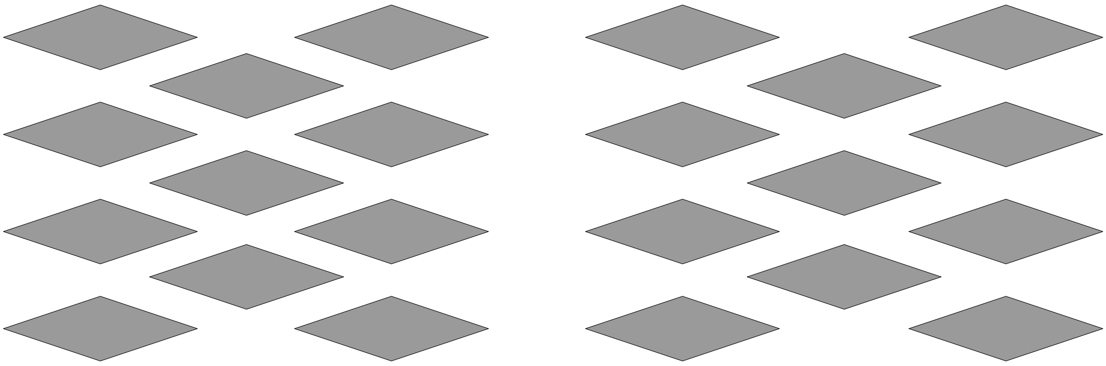

(*a*) Diamond pin fins

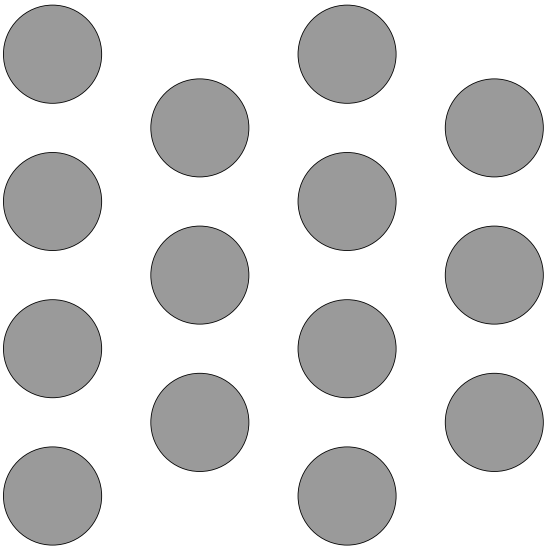

(*b*) Circular pin fins [40]

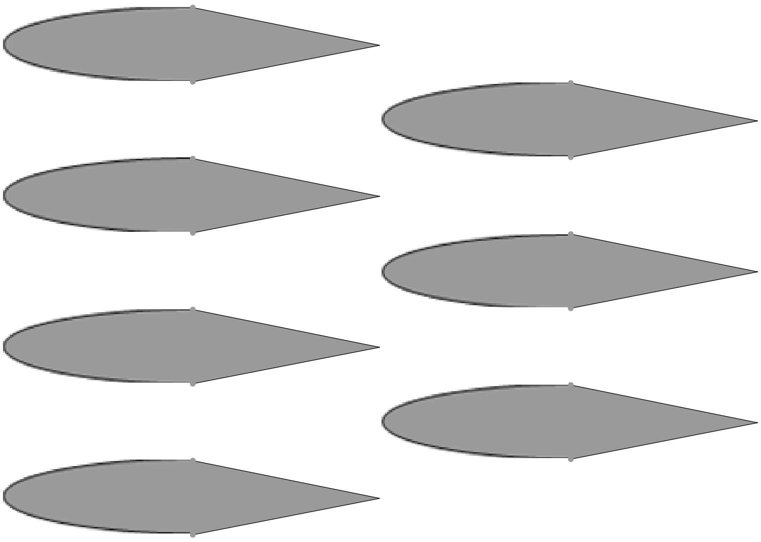

(*c*) Hydrofoil-based pin fins [40]

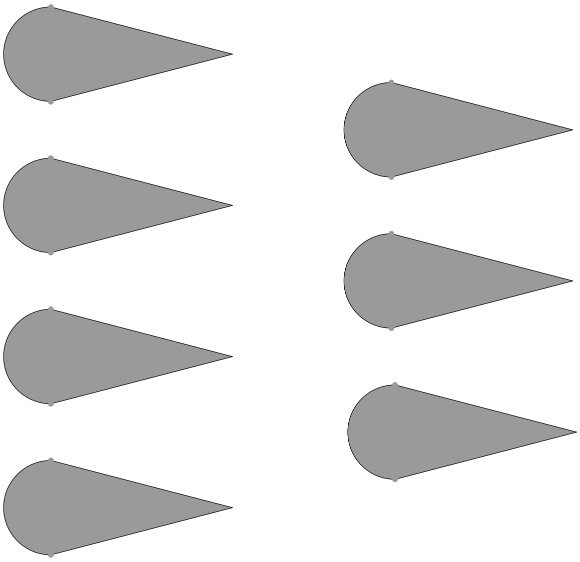

(*d*) Cone-shaped pin fins [40]

Figure 6. 2: Geometry and arrangement of different pin fins

6.2.3 Silicon-to-Glass Wafer Bonding Technology

In this work, silicon-to-silicon wafer bonding was used to seal the channel structures on the top wafer, because comparing to other wafer bonding technologies, it does not require complicated processes [13][41][42]. Silicon-to-silicon wafer bonding can be carried out at a relatively low temperature (400 ºC) and does not induce any by-product materials. However, because silicon wafers are opaque, there is no optical access to the channels and therefore, the boiling behaviour cannot be visually observed. Optical access can be obtained by using silicon-to-glass wafer bonding, and the boiling behaviour in those channels can be monitored through a microscope.

Reference

[1] C. Rops, F. van der Graaf, and J. Velthuis, “Micro evaporators,” *The 2004 International Conference on MEMS, NANO and Smart Systems, 2004. ICMENS 2004. Proceedings.* , 2004, pp. 421-426.

[2] J.D. Heppner, D.C. Walther, and A.P. Pisano, “The design of ARCTIC: A rotary compressor thermally insulated µcooler,” *Sensors and Actuators A: Physical*, vol. 134, Feb. 2007, pp. 47-56.

[3] J. Jung, H. Oh, D.K. Lee, K.B. Choi, S.K. Dong, and H. Kwak, “A capillary-pumped loop (CPL) with microcone-shaped capillary structure for cooling electronic devices,” *Journal of Micromechanics and Microengineering*, vol. 18, 2008, p. 017002.

[4] C. Rops, J. Hao, R. Lindken, M. Mihailovic, J. Creemer, P. Sarro, and J. Westerweel, “Heat transfer enhancement of micro-fabricated fin structures: ultra-compact heat exchanger design,” *Proceedings of GPE-EPIC conference*, Venice: 2009.

[5] P. Dixit, Nay Lin, Jianmin Miao, Wai Kwan Wong, and Kiat Choon Teo, “Concept and analytical analysis of silicon micro/nanopillars based 3-D stacked microchannel heat sink for advanced heat dissipation applications,” *Electronic Components and Technology Conference, 2007. ECTC '07. Proceedings. 57th*, 2007, pp. 1149-1154.

[6] D. Tuckerman and R. Pease, “High-performance heat sinking for VLSI,” *Electron Device Letters, IEEE*, vol. 2, 1981, pp. 126-129.

[7] C. Gillot, L. Meysenc, C. Schaeffer, and A. Bricard, “Integrated single and two-phase micro heat sinks under IGBT chips,” *IEEE Transactions on Components and Packaging Technologies*, vol. 22, 1999, pp. 384-389.

[8] T. Chen and S. Garimella, “Flow boiling heat transfer to a dielectric coolant in a microchannel heat sink,” *IEEE Transactions on Components and Packaging Technologies*, vol. 30, 2007, pp. 24-31.

[9] S. Lee and Weilin Qu, “Thermal design methodology for low flow rate single-phase and two-phase micro-channel heat sinks,” *IEEE Transactions on Components and Packaging Technologies*, vol. 30, 2007, pp. 830-841.

[10] N. Lei, P. Skandakumaran, and A. Ortega, “Experiments and modelling of multilayer copper minichannel heat sinks in single-phase flow,” *The Tenth Intersociety Conference on Thermal and Thermomechanical Phenomena in Electronics Systems, 2006. ITHERM '06.*, 2006, pp. 9-18.

[11] D.R. Lide, “Handbook of chemistry and physics - online,” CRC, 2008.

[12] Weilin Qu and I. Mudawar, “Thermal design methodology for high-heat-flux single-phase and two-phase micro-channel heat sinks,” *IEEE Transactions on Components and Packaging Technologies*, vol. 26, 2003, pp. 598-609.

[13] S. Franssila, “Introduction to microfabrication,” Wiley, 2004.

[14] Y.A. Cengel, “Heat transfer: a practical approach,” McGraw-Hill, 2003, pp. 17-25.

[15] J. Hao, “Ultra-high-speed flash ADC design,” Master Thesis, Southeast University, 2007.

[16] F.P. Incropera, D.P. DeWitt, T.L. Bergman, and A.S. Lavine, “Fundamentals of heat and mass transfer,” Wiley, 2007, pp. 3-6.

[17] C. Kittel, “Introduction to solid state physics,” Wiley, 2004, pp. 121-122.

[18] F.P. Incropera, D.P. DeWitt, T.L. Bergman, and A.S. Lavine, “Fundamentals of heat and mass transfer,” Wiley, 2007, pp. 6-9.

[19] Y.A. Cengel, “Heat transfer: a practical approach,” McGraw-Hill, 2003, pp. 25-27.

[20] Y.A. Cengel, “Heat transfer: a practical approach,” McGraw-Hill, 2003, pp. 27-29.

[21] F.P. Incropera, D.P. DeWitt, T.L. Bergman, and A.S. Lavine, “Fundamentals of heat and mass transfer,” Wiley, 2007, pp. 9-11.

[22] “Fluids - Latent Heat of Evaporation,” *The Engineering ToolBox*.

[23] Y.A. Cengel, “Heat transfer: a practical approach,” McGraw-Hill, 2003, pp. 515-530.

[24] F.P. Incropera, D.P. DeWitt, T.L. Bergman, and A.S. Lavine, “Fundamentals of heat and mass transfer,” Wiley, 2007, pp. 620-632.

[25] Y.A. Cengel, “Heat transfer: a practical approach,” McGraw-Hill, 2003, pp. 530-532.

[26] Y.A. Cengel, “Heat transfer: a practical approach,” McGraw-Hill, 2003, p. 422.

[27] F.P. Incropera, D.P. DeWitt, T.L. Bergman, and A.S. Lavine, “Fundamentals of heat and mass transfer,” Wiley, 2007, pp. 636-640.

[28] S.G. Kandlikar, “Heat transfer mechanisms during flow boiling in microchannels,” *Journal of Heat Transfer*, vol. 126, 2004, pp. 8-16.

[29] W. Qu and I. Mudawar, “Flow boiling heat transfer in two-phase micro-channel heat sinks--II. Annular two-phase flow model,” *International Journal of Heat and Mass Transfer*, vol. 46, Jul. 2003, pp. 2773-2784.

[30] L. Yarin, A. Mosyak, and G. Hetsroni, “Fluid flow, heat transfer and boiling in micro-channels,” Springer, 2009, pp. 281-283.

[31] L. Zhang, K. Goodson, and T. Kenny, “Silicon Microchannel Heat Sinks Theories and Phenomena,” Springer, , p. 78.

[32] S.G. Kandlikar and W.J. Grande, “Evolution of microchannel flow passages - thermohydraulic performance and fabrication technology,” *Proceedings of IMECE2002, ASME International Mechanical Engineering Congress & Exposition*, 2002.

[33] L. Zhang, K. Goodson, and T. Kenny, “Silicon Microchannel Heat Sinks Theories and Phenomena,” Springer, , pp. 82-83.

[34] G. Hetsroni, A. Mosyak, E. Pogrebnyak, and Z. Segal, “Explosive boiling of water in parallel micro-channels,” *International Journal of Multiphase Flow*, vol. 31, Apr. 2005, pp. 371-392.

[35] C. Rops, “Two-phase flow and phase change heat transfer in small structures,” PhD Dissertation, Delft University of Technology, 2009.

[36] D.K. Schroder, “Semiconductor material and device characterization,” Wiley, 2006, p. 9.

[37] J. Aronstein and T. Hare, “AC and DC electromigration failure of aluminum contact junctions,” *IEEE Transactions on Components and Packaging Technologies*, vol. 28, 2005, pp. 701-709.

[38] I. Bahl, “High-performance inductors,” *IEEE Transactions on Microwave Theory and Techniques*, vol. 49, 2001, pp. 654-664.

[39] D.K. Schroder, “Semiconductor material and device characterization,” Wiley, 2006, pp. 2-18.

[40] A. Kosar and Y. Peles, “TCPT-2006-096.R2: Micro scale pin fin heat sinks - parametric performance evaluation study,” *IEEE Transactions on Components and Packaging Technologies*, vol. 30, 2007, pp. 855-865.

[41] M. Schmidt, “Wafer-to-wafer bonding for microstructure formation,” *Proceedings of the IEEE*, vol. 86, 1998, pp. 1575-1585.

[42] Qin-Yi Tong, G. Cha, R. Gafiteanu, and U. Gosele, “Low temperature wafer direct bonding,” *Microelectromechanical Systems, Journal of*, vol. 3, 1994, pp. 29-35.

Acknowledgements

Over the past year, I have benefited from the help, encouragements, and criticism offered by many people. This thesis would not have been possible in its present form without their contributions; and I shall attempt to express my gratitude towards them here.

First and foremost, I would like to thank my supervisor, Prof. P. M. Sarro, for offering me this M.Sc. project. Your warm words always encourage and support me.

I would also like to thank Dr. J. F. Creemer. Your deep scientific insights and serious attitude to research have left a deep impression on me.

My very special thanks go to Marko Mihailović. You helped me in every possible way, more than could have been expected from a mentor.

I am also very grateful to TNO for giving me the opportunity to work on this project, and especially to my mentor Cor Rops from TNO. He helped me a lot in the fluidic part of this project.

I also want to thank Dr. Luigi Mele and Bruno Morana for assisting me in the project, and Silvana Milosavljević, Charles de Boer, and Peter swart for giving me the training in the cleanroom and measurement room.

I am also very graceful to all the technicians from ECTM and TNO for their kindness and help.

Finally, I would like to thank my family and loved ones. They have been always encouraging me and supporting me.